Supporting Information

Geometry and Electronic Structure of $Yb(III)[CH(SiMe_3)_2]_3$ from EPR and solid-state NMR augmented by Computations

Anton Ashuiev,[†] Florian Allouche,[†] Md. Ashraful Islam,[‡] José P. Carvalho,[¶] Kevin J. Sanders,[‡] Matthew P. Conley,[§] Daniel Klose,[†] Giuseppe Lapadula,[†] Michael Wörle,[†] Dirk Baabe,[‖] Marc D. Walter,[‖] Andrew J. Pell,[*,‡] Christophe Copéret,[*,†] Gunnar Jeschke,[*,†] Guido Pintacuda,[*,‡] and Richard A. Andersen[⊥]

[†]*Department of Chemistry and Applied Biosciences, ETH Zurich, Wolfgang-Pauli-Strasse 1-5, 8093 Zurich, Switzerland*

[‡]*Université de Lyon, Centre de RMN à Très Hauts Champs de Lyon (UMR 5082 - CNRS, ENS Lyon, Université Claude Bernard Lyon 1), F-69100 Villeurbanne, France*

[¶]*Department of Materials and Environmental Chemistry, Stockholm University, Svänte Arrhenius väg 16 C 106 91 Stockholm, Sweden*

[§]*Department of Chemistry and Chemical Sciences, University of California Riverside, 501 Big Springs Road, Riverside, CA 92521, USA*

[‖]*Institut für Anorganische und Analytische Chemie, Technische Universität Braunschweig, Hagenring 30, 38106 Braunschweig, Germany*

[⊥]*Department of Chemistry, University of California, Berkeley, CA 94720, USA*

E-mail: andrew.pell@ens-lyon.fr; ccoperet@ethz.ch; gjeschke@ethz.ch; guido.pintacuda@ens-lyon.fr

Table of contents

1 Materials and Methods **S4**

1.1 General procedures S4

1.2 Preparation of $Yb[CH(SiMe_3)_2]_3$ S4

1.3 Preparation of $[O{-}2,6{-}tBu_2{-}C_6H_3]Yb[CH(SiMe_3)_2]_2$ S5

1.4 Preparation of $[O{-}2,6{-}t Bu_2{-}C_6H_3]_2Yb[CH(SiMe_3)_2]$ S6

1.5 Magnetic susceptibility measurements S6

1.6 Solid-state NMR S7

1.7 EPR studies S10

1.8 Quantum chemistry calculations S13

Geometry optimization S13

Electronic structure and magnetic properties S13

2 Crystallographic data **S16**

2.1 $Yb[CH(SiMe_3)_2]_3$ S16

2.2 $Yb[CH(SiMe_3)_2]_{3-n}[O{-}2,6{-}tBu_2{-}C_6H_3]_n$ with n = 1 and 2 . . . . . S19

3 Solution ^{1}H NMR experiments **S25**

4 EPR characterization **S27**

4.1 HYSCORE simulations S27

5 Computational modeling **S28**

5.1 DFT-optimized structure of $Yb[CH(SiMe_3)_2]_3$ S28

5.2 NBO analysis S30

5.3 Prediction of paramagnetic shifts S32

5.4 Modeling molecular dynamics from NMR data S35

6 Magnetic susceptibility studies **S37**

7 NMR characterization of

$Yb[CH(SiMe_3)_2]_{3-x}[O{-}2,6{-}t Bu_2{-}C_6H_3]_x$ (x = 1, 2) complexes **S43**

1 Materials and Methods

1.1 General procedures

All experiments were carried out under dry and oxygen free argon atmosphere using either standard Schlenk or glove-box techniques. Pentane, toluene and diethyl ether were purified using double MBraun SPS alumina columns, and were degassed using three freeze-pump-thaw cycles before being used. All infrared (IR) spectra were recorded using a Bruker Alpha spectrometer placed in a glovebox, using the software OPUS. Solution ^{1}H spectra were obtained on a Bruker DRX 250 spectrometer. The ^{1}H chemical shifts are referenced relative to the residual solvent peak and reported relative to tetramethylsilane (δ = 0 ppm). Cl[CH(SiMe$_3$)$_2$] was ordered from Sigma-Aldrich and used without further purification. Yb(O−2,6−tBu$_2$−C$_6$H$_3$)$_3$[1] and Li[CH(SiMe$_3$)$_2$][2] were synthesized according to literature procedures.

1.2 Preparation of Yb[CH(SiMe$_3$)$_2$]$_3$

Yb(O−2,6−tBu$_2$−C$_6$H$_3$)$_3$ (1.06 g, 1.34 mmol) was dissolved in 50 mL of pentane to give a red solution. A solution of Li[CH(SiMe$_3$)$_2$] (0.704 g, 4.23 mmol, 3.15 equiv) was dissolved in a mixture of pentane (90 mL) and toluene (10 mL), and the solution was added to the solution of Yb(O−2,6−tBu$_2$−C$_6$H$_3$)$_3$ at 20°C dropwise over ca. 90 min using an addition funnel. During the course of the reaction the color changed from red (Yb(O−2,6−tBu$_2$−C$_6$H$_3$)$_3$ and Yb[CH(SiMe$_3$)$_2$][(O−2,6−tBu$_2$−C$_6$H$_3$)]$_2$ are both red) to brown (Yb[CH(SiMe$_3$)$_2$]$_2$[(O−2,6−tBu$_2$−C$_6$H$_3$)]) to blue (Yb[CH(SiMe$_3$)$_2$]$_3$), as a thick-white precipitate formed. The mixture was stirred at room temperature for 16 h. The volatile materials were removed under reduced pressure, resulting in a light blue solid. Pentane (30 mL) was added by cannula to give a blue solution and an insoluble white precipitate, which was separated by filtration. The clear blue pentane solution was concentrated at room

temperature under vacuum to ca. 10 mL and cooled to −40°C. Large blue blocky needles of the product were isolated in four crops by filtration. Yield 0.490 g (56 %). The needles contain 0.25 equiv of $CH_2(SiMe_3)_2$ as deduced by the solution ^{1}H NMR spectrum ($\delta(SiCH_3)$= 0.01 ppm and $\delta(CH_2)$= -0.42 ppm) and elemental analysis. ^{1}H NMR (C_6D_6, 25 ° C): 29.4 ppm, $\nu_{1/2}$= 1290 Hz. Elemental Analysis: Calculated for $C_{21}H_{57}Si_6Yb$: C, 38.73; H, 8.82. Found: C, 39.84; H, 8.86.

1.3 Preparation of [O−2,6−tBu$_2$−C$_6$H$_3$]Yb[CH(SiMe$_3$)$_2$]$_2$

Yb(O−2,6−tBu$_2$−C$_6$H$_3$)$_3$ (0.800 g, 1.02 mmol) was dissolved in 25 mL of pentane to give a red solution. A solution of Li[CH(SiMe$_3$)$_2$] (0.372 g, 2.24 mmol, 2.2 equiv) dissolved in a mixture of pentane (90 mL) and toluene (10 mL) was added to the solution of Yb(O−2,6−tBu$_2$−C$_6$H$_3$)$_3$ at 20°C dropwise over ca. 45 min using an addition funnel. During the course of the reaction the color changes from red (Yb(O−2,6−tBu$_2$−C$_6$H$_3$)$_3$ and [O−2,6−tBu$_2$−C$_6$H$_3$]$_2$Yb[CH(SiMe$_3$)$_2$] are red) to brownish purple (a mixture of brown [O−2,6−tBu$_2$−C$_6$H$_3$]Yb[CH(SiMe$_3$)$_2$]$_2$ and blue Yb[CH(SiMe$_3$)$_2$]$_3$). A thick-white precipitate also formed. The mixture was stirred at room temperature for 16 h. The volatile materials were removed under reduced pressure, resulting in a brown solid. Pentane (50 mL) was added by cannula to form a brown solution and an insoluble white precipitate, which was removed by filtration. The clear brown pentane solution was concentrated to ca. 30 mL and placed at −40°C. Large brown blocks of the product were isolated by filtration. Yield 0.130 g (21 %). ^{1}H NMR (C_6D_6, 25 °C, recycling delay of 0.5 s): 68.6 ppm, $\nu_{1/2}$= 2560 Hz, relative area 13, −18.7 ppm, $\nu_{1/2}$= 37 Hz, relative area 1.8, −21.0 ppm, $\nu_{1/2}$= 68 Hz, relative area 1. Elemental Analysis: Calculated for $C_{28}H_{59}OSi_4Yb$: C, 48.24; H, 8.53. Found: C, 47.96; H, 8.21.

1.4 Preparation of $[O{-}2,6{-}t\mathrm{Bu}_2{-}\mathrm{C}_6\mathrm{H}_3]_2\mathrm{Yb}[\mathrm{CH}(\mathrm{SiMe}_3)_2]$

$\mathrm{Yb}(O{-}2,6{-}t\mathrm{Bu}_2{-}\mathrm{C}_6\mathrm{H}_3)_3$ (1.22 g, 1.54 mmol) was dissolved in 30 mL of pentane to give a red solution. A solution of $\mathrm{Li}[\mathrm{CH}(\mathrm{SiMe}_3)_2]$ (0.281 g, 1.70 mmol, 1.1 equiv) was dissolved in a mixture of pentane (100 mL) and toluene (5 mL), and the solution was added to the solution of $\mathrm{Yb}(O{-}2,6{-}t\mathrm{Bu}_2{-}\mathrm{C}_6\mathrm{H}_3)_3$ at 20°C dropwise over ca. 45 min using an addition funnel. The solution maintained the red color and a thick white precipitate formed. The mixture was stirred at room temperature for 16 h. The volatile material was removed under reduced pressure, resulting in a red solid. Pentane (50 mL) was added by cannula to form a red solution and an insoluble white precipitate, which was separated by filtration. The clear red pentane solution was concentrated to ca. 15 mL and placed at 4°C. Red blocks of the product were isolated by filtration in two crops. Yield 0.401 g (35 %). ^{1}H NMR ($\mathrm{C}_6\mathrm{D}_6$, 25°C, recycling delay of 0.5 s): 78.2 ppm, $\nu_{1/2}$= 5760 Hz, relative area 1.4, 42.0 ppm, $\nu_{1/2}$= 3226 Hz, relative area 9.3, -17.4 ppm, $\nu_{1/2}$= 136 Hz, relative area 1.6, -18.9 ppm, $\nu_{1/2}$= 64 Hz, relative area 1. Elemental Analysis: Calculated for $\mathrm{C}_{35}\mathrm{H}_{61}\mathrm{O}_2\mathrm{Si}_2\mathrm{Yb}$: C, 56.57; H, 8.27. Found: C, 56.79; H, 8.31.

1.5 Magnetic susceptibility measurements

Solid-state magnetic susceptibility studies on polycrystalline powders of $\mathrm{Yb}[\mathrm{CH}(\mathrm{SiMe}_3)_2]_{3-x}[O{-}2,6{-}t\mathrm{Bu}_2{-}\mathrm{C}_6\mathrm{H}_3]_x$ with $x = 0, 1, 2, 3$ were performed. The samples were prepared in quartz tubes as previously described.[3] The data were recorded on a Cryogenic Ltd. closed-cycle SQUID magnetometer between 2.6 and 300 K with an applied magnetic field of 1 kOe. The diamagnetic background signal of the empty sample holder including quartz wool was experimentally determined and subtracted from the raw magnetization data. The experimental data were also corrected for the overall diamagnetism of the investigated molecules using tabulated Pascal constants.[4]

1.6 Solid-state NMR

Natural abundance solid-state ^{1}H, ^{13}C, and ^{29}Si NMR spectra of Yb[CH(SiMe$_3$)$_2$]$_3$ were acquired on a Bruker Avance III spectrometer operating at an external magnetic field strength of 11.74 T (corresponding to a Larmor frequencies of 500.16 MHz, 125.7 MHz, and 99.44 MHz for ^{1}H, ^{13}C, and ^{29}Si, respectively) using a Bruker HX 2.5 mm wide-bore magic-angle spinning (MAS) probe. In all cases the powdered sample was packed in a standard 2.5 mm ZnO_2 rotor in an Ar-filled glovebox, then placed in a sealed glass tube before removal from the glovebox in order to protect the sample from atmosphere. Immediately before measurement, the sealed tube was opened and the rotor was quickly inserted in to the MAS probe, and simultaneously spun up to the desired rotation rate while cooling the stator to a sample temperature of approximately 300 K using a Bruker BCU XTreme cooling unit. Nitrogen gas dried to a dew point of -80°C was used for sample rotation.

The natural abundance ^{1}H, ^{13}C, and ^{29}Si MAS NMR spectra were acquired using the double spin echo (Figure S1(a)). The 1D MAS spectrum of ^{1}H and ^{29}Si was acquired using a MAS rotation rate of 30 kHz (corresponding to a rotor period of 33.33 μs) and tanh/tan SHAP pulses with a length of 33.33 μs. Both excitation and refocusing pulses employed an RF field strength of $\nu_{1,max}$= 147 and 114 kHz and a recycle delay of 0.5 s and 0.036 s, respectively. The 1D MAS spectrum of ^{13}C was acquired using a MAS rotation rate of 14.286 kHz (corresponding to a rotor period of 70 μs) and tanh/tan SHAP pulses with a length of 70.00 μs and a recycle delay of 0.03 s. Both excitation and refocusing pulses employed an RF field strength of $\nu_{1,max}$= 118 kHz, respectively.

The adiabatic magic-angle turning (aMAT)[5] experiment shown in Figure S1(b), was used to obtain 2D isotropic-anisotropic correlation spectra of ^{1}H, ^{13}C and ^{29}Si. For ^{1}H, an MAS rotation rate of 30 kHz was used with a recycle delay of 0.01 s, 32 scans per increment and 280 t_1 increments acquired in steps of 3.1 μs. The pulses were identical to those used in the 1D MAS spectra. An MAS rotation rate of 20 kHz was used for both ^{13}C and ^{29}Si, 33.33 μs

tanh/tan SHAP pulses were employed for refocusing. Both excitation and refocusing pulses employed an RF field strength of $\nu_{1,max}$= 118 kHz, a recycle delay of 0.036 s, and 24576 and 45056 scans per increment, respectively. 36 t_1 increments were acquired in steps of 27.78 μs. All projections in the indirect dimension were fitted with asymmetric Gaussian functions:

$$f(\nu_1) = A\frac{\exp\left[-\frac{1}{2}\left(\frac{\omega-\mu}{\sigma}\right)^2\right]}{\sqrt{2\pi}\sigma}\,\mathrm{erfc}\left[-\frac{\alpha(x-\mu)}{\sqrt{2}\sigma}\right] \tag{1}$$

where A, μ, σ are the amplitude, mean and standard deviation of the Gaussian function, α is a scale factor and erfc is the complex error function. The mean and standard deviation of distribution are given by:

$$\mu_{\mathrm{asym,gaus}} = \mu + \frac{\sqrt{(\frac{2}{\pi})}\alpha\sigma}{\sqrt{(1+\alpha^2)}} \tag{2}$$

$$\sigma_{\mathrm{asym,gaus}} = \sigma\sqrt{1 - \frac{2\alpha^2}{\pi(1+\alpha^2)}} \tag{3}$$

Heteronuclear correlation (HETCOR) spectroscopy between ^{1}H and ^{13}C was achieved by using a HETCOR variant of the transferred-echo double resonance (TEDOR)[6] experiment Figure S1(c). The MAS rotation rate was 30 kHz and the ^{1}H and ^{13}C pulses used RF field strengths of 250 kHz and 111 kHz, respectively.

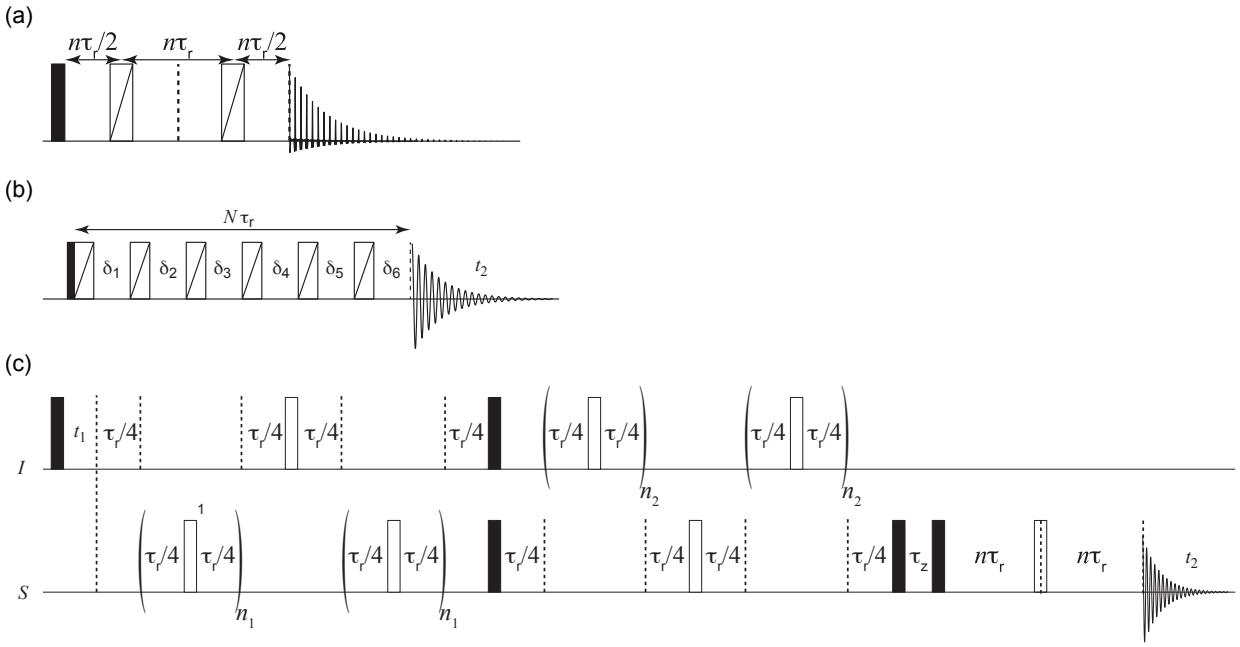

Figure S1: (a) The double spin echo pulse sequence, where n represents an integer multiple of rotor periods τ_r. The sequence employs SHAPs,[7] for refocusing the chemical shift evolution, using the tanh/tan frequency-swept pulse shape a. (b) The 2D aMAT[5] sequence used in this study, with an evolution time of N rotor periods. N was set large enough to fully evolve the isotropic evolution. (c) The HETCOR variant of the TEDOR sequence.[6] Filled rectangles indicate pulses with a nominal flip angle of 90°, unfilled rectangles indicate a 180° pulse, and unfilled rectangles with a diagonal stroke indicate SHAPs.

1.7 EPR studies

All EPR measurements were performed in X band (microwave frequency ca. 9.5 GHz) due to high anisotropy of the g tensor. For all CW and pulse EPR experiments, the solid powder of $Yb[CH(SiMe_3)_2]_3$ was ground together with the solid powder of $Lu[CH(SiMe_3)_2]_3$ with a molar ratio 5:95, respectively. The obtained powder was flame-sealed into quartz EPR tubes under high vacuum.

The CW EPR spectrum of $Yb[CH(SiMe_3)_2]_3$ (Figure 3a of the main text) was recorded at a temperature of 10 K on an Elexsys E680 EPR spectrometer (Bruker Biospin, Rheinstetten, Germany), equipped with a helium flow cryostat ESR900 (Oxford Instruments, Oxfordshire, UK). The measurement was performed using a Bruker Super-High-Q resonator, with a modulation amplitude of 0.4 mT and a modulation frequency of 100 kHz. The lock-in amplifier time constant and conversion time were set to 40.96 ms and 81.92 ms, respectively. The magnetic field offset was corrected using 2,2-diphenyl-1-picrylhydrazyl (Sigma-Aldrich, Buchs, Switzerland) as a standard. The obtained spectrum was simulated (Figure 3a, red), using EasySpin.[8]

The echo-detected EPR spectrum of $Yb[CH(SiMe_3)_2]_3$ (Figure 3b of the main text) was recorded at a temperature of 3.8 K on a Bruker Elexsys E680 EPR spectrometer, equipped with a helium flow cryostat CF935 (Oxford Instruments, Oxfordshire, UK), using a Bruker MS-3 split-ring resonator. The spectrum was recorded using a standard 2-pulse Hahn Echo sequence, $\pi/2 - \tau - \pi - \tau -$ echo, with the power of the microwave pulses set up for pulse lengths of $t_{\pi/2} = 16$ ns, $t_\pi = 32$ ns. The interpulse delay was set to $\tau = 128$ ns.

Subsequently, the ELDOR-detected NMR (EDNMR)[9] spectrum of $Yb[CH(SiMe_3)_2]_3$ (Figure 3d of the main text) was recorded at the field position corresponding to the maximum echo intensity. The standard EDNMR pulse sequence HTA$-t_0-\pi/2-\tau-\pi-\tau-$echo (HTA: high turning angle pulse) was used, with $t_{HTA} = 1500$ ns, $\tau_{\pi/2} = 16$ ns, $t_\pi = 32$ ns, $t_0 = 1000$ ns, and $\tau = 300$ ns. The frequency of the HTA pulse was swept in a range of ± 300

MHz around the spectrometer frequency of ca. 9.35 GHz in steps of 250 kHz. The microwave power of the HTA pulse was attenuated by 30 dB. The final ^{1}H EDNMR spectrum, shown in Figure 3d of the main text, was obtained by subtraction of a linear baseline in the region 23−57 MHz.

For HYSCORE experiments, the standard 4-pulse sequence $\pi/2-\tau-\pi/2-t_1-\pi-t_2-\pi/2-\tau-$echo with pulse lengths $\tau_{\pi/2}$ = 12 ns, τ_π = 8 ns was used with time steps Δt_1 and Δt_2 set to 8 ns. An eight-step phase cycle was used to remove unwanted echo contributions. The repetition rate was set to 2 kHz. The length of HYSCORE traces was set to 2160 ns in both dimensions. The magnetic field position for HYSCORE measurements, indicated in Fig. 3a and b of the main text with black arrows, was selected due to a better modulation depth, observed in the HYSCORE time traces at this position compared to the spectral maximum. The final spectrum (Figure 3c of the main text and Figure 7) was obtained via summation of HYSCORE spectra with τ = 96 ns, τ = 112 ns and τ = 144 ns to compensate for blind spots. A Lorentz-to-Gauss transformation (τ = 0.15, σ = 0.5) of the time-domain signal was applied before Fourier transformation in order to enhance the spectral resolution.

The numerical simulation of the HYSCORE spectrum was performed in EasySpin[8] using the function *saffron*, with manually estimated parameters of ^{1}H hyperfine coupling as input. The spectrum was simulated (Figure 3c of the main text) for interpulse delays τ = 96 ns, τ = 112 ns and τ = 144 ns, assuming a bandwidth of the microwave pulses of 125 MHz. With the excitation bandwidth included in the numerical simulation, the lineshape of the simulated HYSCORE pattern appeared to be sensitive to the orientation of principal axes frame (PAF) of the hyperfine coupling tensors with respect to the z axis of the PAF of the g tensor. The parameters of hyperfine couplings are described by principal values of hyperfine tensors in the form

$$A = a_{\text{iso}} + a_{\text{dip}} = [a_{\text{iso}} + a_{\text{dip(1)}}; a_{\text{iso}} + a_{\text{dip(2)}}; a_{\text{iso}} + a_{\text{dip(3)}}]. \quad (4)$$

In the simulation, an axial ^{1}H hyperfine tensor with $a_{\mathrm{dip}} = [-T_{\mathrm{dip}}; -T_{\mathrm{dip}}; 2\,T_{\mathrm{dip}}]$ was assumed. The tensor parameters (see main text) were determined by visual comparison of the experimental and simulated HYSCORE spectra.

1.8 Quantum chemistry calculations

Geometry optimization

The geometry optimization was performed using the program ORCA 5.0.1[10] with an increased accuracy of numerical integration (orca keyword defgrid3, in particular with a strongly increased radial integration accuracy for Yb atom (orca keyword SpecialGridIntAcc 12) and very tight SCF convergence criteria, (orca keyword verytightscf). The optimization was carried out considering the unrestricted DFT method employing the hybrid PBE0 functional[11–13] and Grimme's D3BJ dispersion correction.[14] Relativistic effects have been introduced with scalar relativistic ZORA Hamiltonian[15] together with Pantazis' all-electron SARC-ZORA-TZVP[16] basis set for the Yb atom and the relativistically recontracted ZORA-def2-TZVP[17] basis set for all other atoms. The Autoaux feature was used for the auxiliary basis sets and resolution of identity (RI) with the chain of spheres approximation was employed (orca keyword RIJCOSX).[18,19] Tight geometry optimization criteria were considered (orca keyword tightopt). Analytical computation of the harmonic vibrational frequencies was also carried out and no vibrational modes with imaginary frequencies were obtained, thus ensuring that the optimized geometry corresponds to local minimum of the potential energy surface.

Electronic structure and magnetic properties

Complete active space (CAS) based multiconfigurational electronic structure calculations were performed on the XRD and DFT optimized structures using openmolcas and ORCA 5.0.1 quantum chemistry software.[10,20,21] SF-CASSCF (spin-free complete active space self consistent field)[22] calculations were performed using the active space consisting of the seven $4f$ orbitals of the Yb(III). Dynamic electron correlation was added using the MS-CASPT2 (multi-state complete active space perturbation theory at 2nd order)[23] method. Relativistic effects at scalar and spin-orbit (SO) levels were included with the DKH2 (Douglas-Kroll-Hess

at 2nd order) Hamiltonian.[24] Spin orbit coupling was calculated as state interaction between the spin-free (SF) states with the RASSI (restricted active space state interaction) module in openmolcas[25] and via quasi-degenerate perturbation thoery (QDPT) in ORCA.[26] SO integrals were calculated in the mean field theory using the AMFI (atomic mean-field integrals) approximation[27] in openmolcas and through spin-orbit mean-field (SOMF) representation of the SOC operator in ORCA.[28,29] In openmolcas, relativistically contracted ANO-RCC (atomic natural orbital) basis sets were used for the calculation with TZP quality for the central Yb and Si atoms, DZP quality for C atoms and DZ quality for H atoms.[30,31] Magnetic susceptibilities were calculated according to the method of Vancoillie et al.[32] and the thermal average of electron spin polarization is calculated by turning off the orbital contribution to the magnetization. Crystal field parameters are calculated according to the ITO procedure in Ref.[33] In ORCA, the relativistic variant SARC-DKH-TZVP basis set was used for the central metal atom while IGLO-III[34] basis sets were utilized for the ligand atoms to calculate hyperfine tensors from SO-CASSCF wave functions in the effective Hamiltonian theory and a Gaussian nuclear model.

Unrestricted DFT based hyperfine tensors for ^{171}Yb were calculated with PBE0 functional in ORCA 5.0.1 program. Relativistic effects were included with ZORA (zeroth order regular approximations) Hamiltonian at scalar (SR) and spin-orbit level. Spin orbit coupling effects were introduced as perturbation through coupled-perturbed self-consistent field (CP-SCF) procedure. SARC-ZORA-TZVP basis set was used for Yb with SARC/J auxiliary basis sets and IGLO-III basis sets were used for the ligand atoms as the inner core orbitals are highly augmented to the nucleus, which is required for accurate evaluation of the Fermi-contact coupling.

Orbital chemical shielding tensors are calculated using the scalar relativistic ZORA-DFT method employing PBE0 functionals and TZVP basis in the GIAO formalism.[35–37]

Natural bond orbital (NBO) analysis[38] was performed in NBO 7 program.[39] The molecular orbital set for the NBO analysis was generated in ORCA, using the PBE0 functional

and DKH2 Hamiltonian, together with the all-electron quadruple-zeta quality SARC2-DKH-QZVP basis set for Yb and relativistically recontracted basis sets DKH-DEF2-TZVP basis set for all the other atoms. Energies of secondary interactions that involve the selected natural orbital were calculated using the "deletion" procedure of the NBO program.[39]

Quantum theory of atoms in molecules (QTAIM) topological analysis have been performed using a modified version of TopChem program packages using the total density.[40] High-quality electron density is usually required to perform this kind of analysis. For this reason, the electron density cube files were generated with $400 \times 400 \times 400$ points. It has been shown that the inclusion or exclusion of spin-orbit coupling in the analysis of electronic density yields similar results; the spin-orbit coupling has minimal impact on structural and bonding analyses as it blends states with similar electronic densities.[41]

2 Crystallographic data

Single crystals suitable for X-ray diffraction were selected under a microscope with polarized light. The data collections were performed at 100 K. For structure solution and refinement, the programs SHELXT and SHELXL embedded in the OLEX2 program suite were used.[42–45] Details of the structure determinations are given in Tables S1, S3 and S5. CCDC 2237830 - 2237832 contain the supplementary crystallographic data for this paper. These data can be obtained free of charge from the Cambridge Crystallographic Data Centre via www.ccdc.cam.ac.uk/structures .

2.1 $Yb[CH(SiMe_3)_2]_3$

The $Yb[CH(SiMe_3)_2]_3$ complex was characterized by X-ray structure analysis (Figure S2). All the crystallographic parameters are summarized in Table S1. Figure S2 shows a view of the molecule. The structure contains 0.5 solvent molecules per complex molecule which are highly disordered along the c-axis. The disordered solvent is described by partially occupied $(Me_3Si)_2CH_2$ with all isotropic displacement parameters set equal and using distance restraints. All hydrogen atoms, with exception of the ones belonging to the solvent molecules, were found in the difference Fourier map and refined freely. Table S1 provides also the comparison between selected distances and angles of the paramagnetic $Yb[CH(SiMe_3)_2]_3$ complex and its diamagnetic analogue $Lu[CH(SiMe_3)_2]_3$.[46]

Table S1: Crystal data and structure refinement for $Yb[CH(SiMe_3)_2]_3$.

Empirical formula	C_{25} H_{57} $Si_{6.8}$ Yb
Formula weight	731.45
Temperature [K]	100.00
Crystal system	trigonal
Space group	$P31c$
a [Å]	16.1800(8)
b [Å]	16.1800(8)
c [Å]	8.5692(4)
α [°]	90
β [°]	90
γ [°]	120
Volume[Å^3]	1942.8(2)
Z	2
ρ_{calc} [cm^3]	1.250
μ [mm^{-1}]	2.635
F(000)	764.0
Crystal size [mm^3]	$0.1 \times 0.08 \times 0.07$
Radiation	MoKα ($\lambda = 0.71073$)
2Θ range for data collection [°]	2.906 to 61.044
Index ranges	$-23 \leq h \leq 23$, $-22 \leq k \leq 22$, $-12 \leq l \leq 12$
Reflections collected	29458
Independent reflections	3935 [$R_{\mathrm{int}} = 0.0373$, $R_\sigma = 0.0312$]
Data/restraints/parameters	3935/69/189
Goodness-of-fit on F^2	1.036
Final R indexes [$I \geq 2\sigma(I)$]	$R_1 = 0.0175$, $wR_2 = 0.0351$
Final R indexes [all data]	$R_1 = 0.0197$, $wR_2 = 0.0359$
Largest diff. peak/hole / [e Å^{-3}]	0.85/-0.587
Flack parameter	0.003(4)

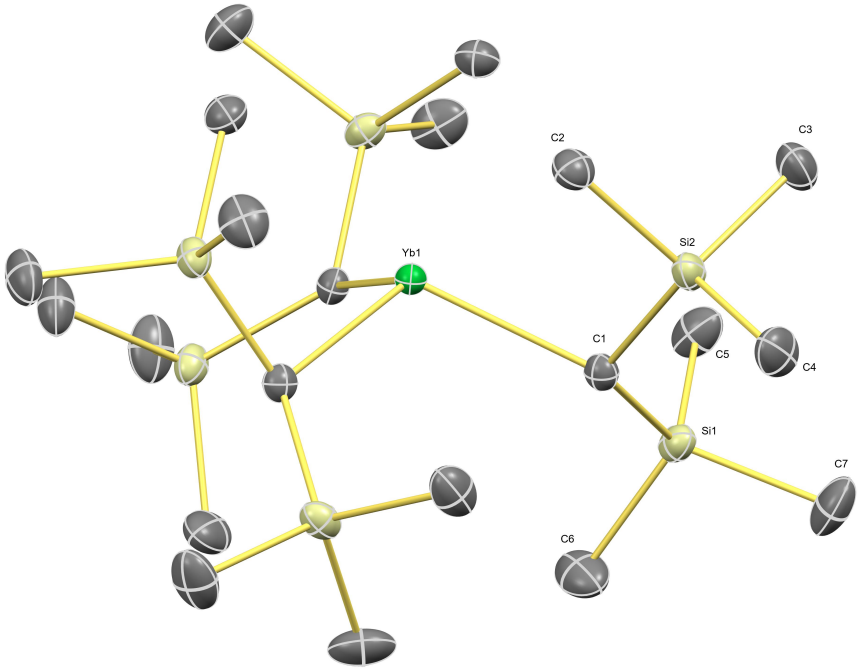

Figure S2: Displacement ellipsoid plot at 50% probability level of $Yb[CH(SiMe_3)_2]_3$. Hydrogen atoms have been omitted for clarity.

Table S2: Comparison of selected bond lengths and angles for $Yb[CH(SiMe_3)_2]_3$ and $Lu[CH(SiMe_3)_2]_3$.[46] The C(1)–Yb–C(1') angle is equal to 109.25(7)°.

	Distances [Å]								
Atoms	M–C(1)	M–C(2)	M–Si(1)	M–Si(2)	Si(2)–C(1)	Si(2)–C(2)	Si(2)–C(3)	Si(1)–C(1)	Si(1)–C(5)
Yb	2.324(3)	2.963(4)	3.7096(8)	3.2596(8)	1.843(3)	1.905(3)	1.869(3)	1.846(3)	1.870(4)
Lu	2.319(3)	2.937(3)	3.7113(8)	3.242(1)	1.837(3)	1.907(3)	1.876(7)	1.844(3)	1.872(5)

	Angle [°]				
Atoms	M–C(1)–Si(1)	M–C(1)–Si(2)	M–C(2)–Si(2)	M–C(1)–C(2)	C(1)–Si(2)–C(2)
Yb	125.25(14)	102.32(13)	80.91(11)	66.07(9)	106.80(14)
Lu	125.7(1)	101.9(1)	81.0(1)	68.6(1)	106.7(1)

2.2 $Yb[CH(SiMe_3)_2]_{3-n}[O-2,6-tBu_2-C_6H_3]_n$ with n = 1 and 2

Table S3: Crystal data and structure refinement for $Yb[CH(SiMe_3)_2]_2[O-2,6-tBu-C_6H_3]$*.

Empirical formula	$C_{28}H_{59}OSi_4Yb$
Formula weight	697.15
Temperature [K]	100
Crystal system	triclinic
Space group	P-1
a [Å]	12.7256(7)
b [Å]	13.6737(7)
c [Å]	20.4896(11)
α [°]	89.3522(8)
β [°]	89.6376(8)
γ [°]	89.7839(8)
Volume[Å^3]	3565.0(3)
Z	4
ρ_{calc} [cm^3]	1.299
μ [mm^{-1}]	2.775
F(000)	1444.0
Crystal size [mm^3]	$0.1 \times 0.09 \times 0.08$
Radiation	MoKα ($\lambda = 0.71073$)
2Θ range for data collection [°]	1.988 to 63.136
Index ranges	$-17 \leq h \leq 18$, $-20 \leq k \leq 20$, $-28 \leq l \leq 28$
Reflections collected	56510
Independent reflections	21831 [$R_{int} = 0.0367$, $R_\sigma = 0.0508$]
Data/restraints/parameters	21831/6/743
Goodness-of-fit on F^2	1.026
Final R indexes [$I \geq 2\sigma(I)$]	R1 = 0.0394, wR2 = 0.0747
Final R indexes [all data]	R1 = 0.0678, wR2 = 0.0862
Largest diff. peak/hole / [e Å^{-3}]	1.96/-1.58

* All hydrogen atoms were found in the difference Fourier map. Hydrogen atoms of methyl groups with large distances to the metal atom were placed at calculated positions and refined according to the riding model. Hydrogen atoms close to the metal center were refined freely with exception of the hydrogen atoms at C8B and C8AB. The hydrogen atom at the carbon atom C8AB with an occupancy of about 30 % cannot be located from the difference density map and has therefore been placed at a calculated position and refined using the riding

model. One $SiMe_3$ group in each of the two crystallographically independent molecules is disordered over two sites and has been described by split positions.

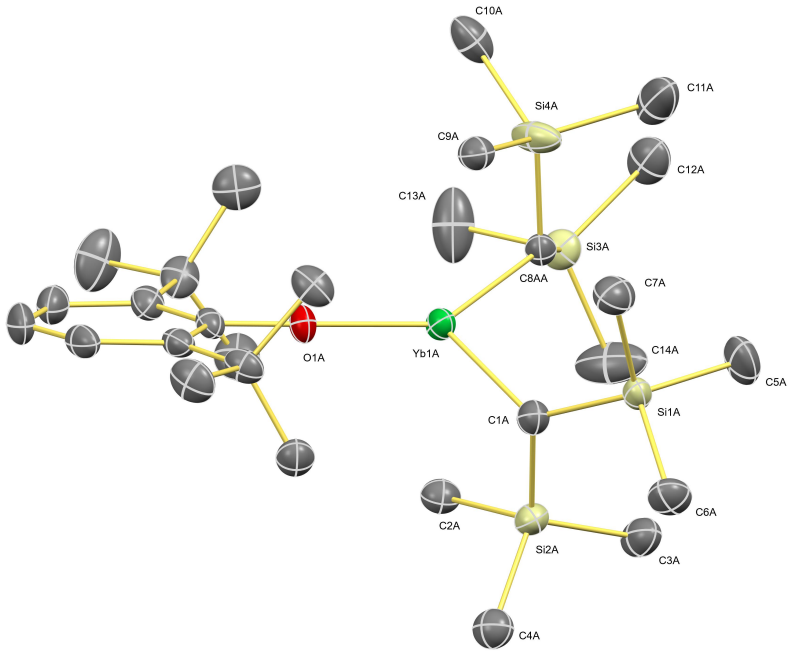

Figure S3: Displacement ellipsoid plot at 50% probability level of $Yb[CH(SiMe_3)_2]_2[O{-}2,6{-}t\mathrm{Bu}{-}C_6H_3]$. Hydrogen atoms as well as the minority orientation of two disordered $SiMe_3$ groups have been omitted for clarity.

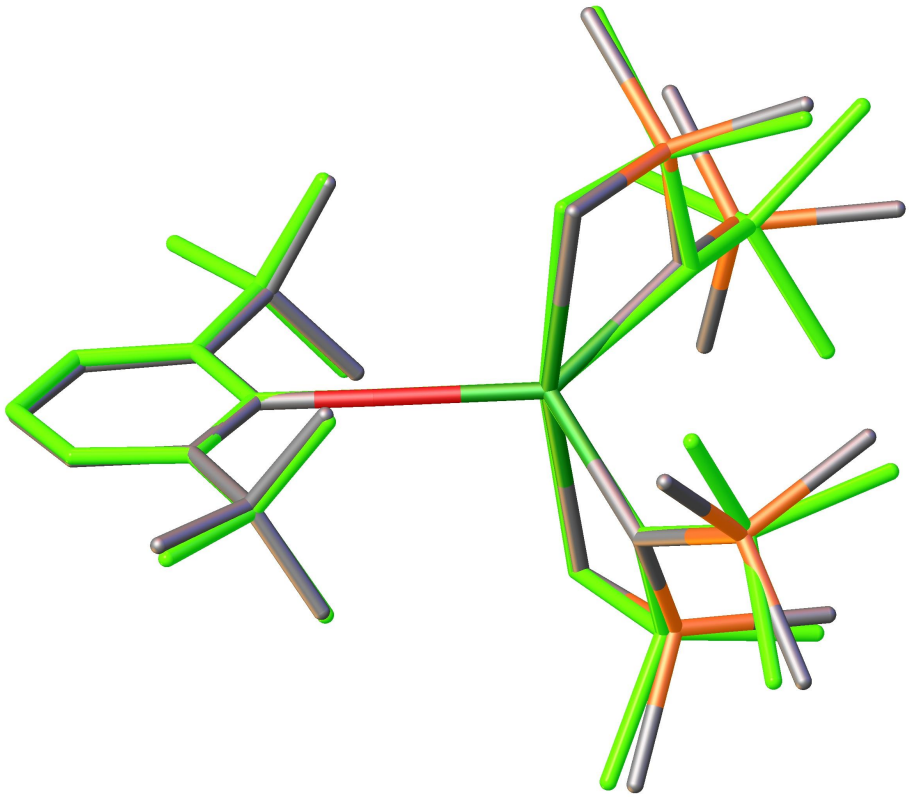

Figure S4: Overlay of both crystallographically independent molecules of $Yb[CH(SiMe_3)_2]_2[O{-}2,6{-}t\text{Bu}{-}C_6H_3]$ in the asymmetric unit. In molecules one of the $SiMe_3$ groups is disordered over two sites. Only the orientation with the larger occupancy factor is shown.

Table S4: Selected interatomic distances for $Yb[CH(SiMe_3)_2]_2[O{-}2,6{-}t\text{Bu}{-}C_6H_3]$.

Atom 1	Atom 2	Distances in molecule A [Å]	Distances in molecule B [Å]
Yb1	Si2	3.1076(10)	3.1291(10)
Yb1	Si4	3.1029(11)	3.1266(10)
Yb1	O1	2.035(2)	2.033(2)
Yb1	C1	2.333(4)	2.329(3)
Yb1	C2	2.712(4)	2.761(4)
Yb1	C9	2.698(4)	2.706(4)
Yb1	C8A	2.340(5))	2.329(3)

Table S5: Crystallographic data of Yb[CH($SiMe_3$)$_2$][O−2,6−tBu−C_6H_3]$_2$*.

Empirical formula	$C_{35}H_{61}O_2Si_2Yb$
Formula weight	743.05
Temperature [K]	100.6(8)
Crystal system	triclinic
Space group	P-1
a [Å]	12.6785(3)
b [Å]	14.3864(3)
c [Å]	22.0939(5)
α [°]	106.806(2)
β [°]	102.024(2)
γ [°]	90.3602(19)
Volume[Å^3]	3763.58(16)
Z	4
ρ_{calc} [cm^3]	1.311
μ [mm^{-1}]	2.575
F(000)	1540.0
Crystal size [mm^3]	$0.25 \times 0.2 \times 0.1$
Radiation	MoKα ($\lambda = 0.71073$)
2Θ range for data collection [°]	3.034 to 56.564
Index ranges	$-16 \leq h \leq 16$, $-19 \leq k \leq 19$, $-29 \leq l \leq 29$
Reflections collected	79428
Independent reflections	18679 [$R_{int} = 0.0711$, $R_\sigma = 0.0621$]
Data/restraints/parameters	18679/88/766
Goodness-of-fit on F^2	1.092
Final R indexes [$I \geq 2\sigma(I)$]	R1 = 0.0584, wR2 = 0.1398
Final R indexes [all data]	R1 = 0.0761, wR2 = 0.1509
Largest diff. peak/hole / [e Å^{-3}]	3.85/-2.26

* The crystal under investigation turned out to be twinned with twin matrix -1 0 0 0 1 0 0 -0.89 -1 with a volume ratio of the individuals of 97:3. The twinning as well as some icing causes relatively large residual electron density peaks. The asymmetric unit contains two crystallographically independent molecules. The hydrogen atoms at C1A and C1B were refined freely, all other were placed at calculated positions and refined according to the riding model.

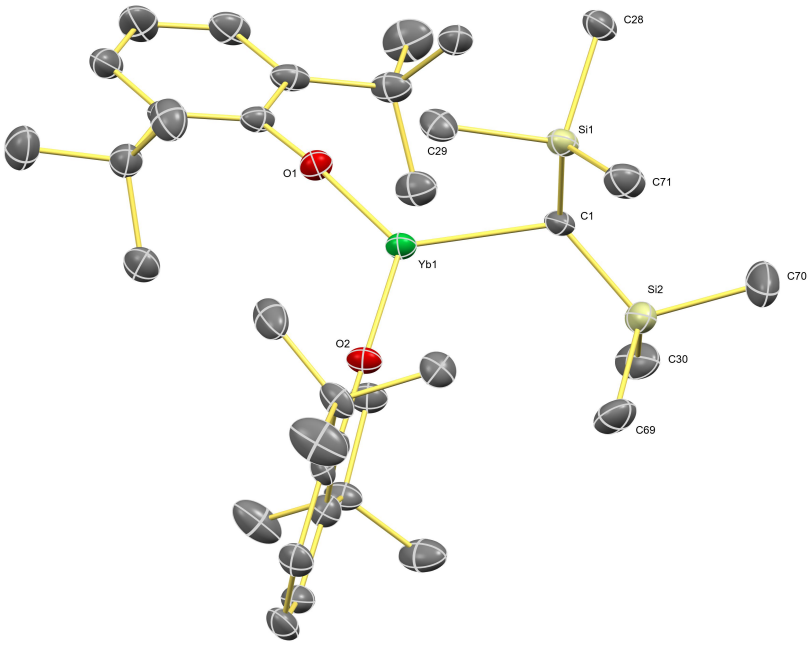

Figure S5: Displacement ellipsoid plot at 50% probability level of $Yb[CH(SiMe_3)_2][O{-}2,6{-}t\text{Bu}{-}C_6H_3]_2$. Hydrogen atoms have been omitted for clarity.

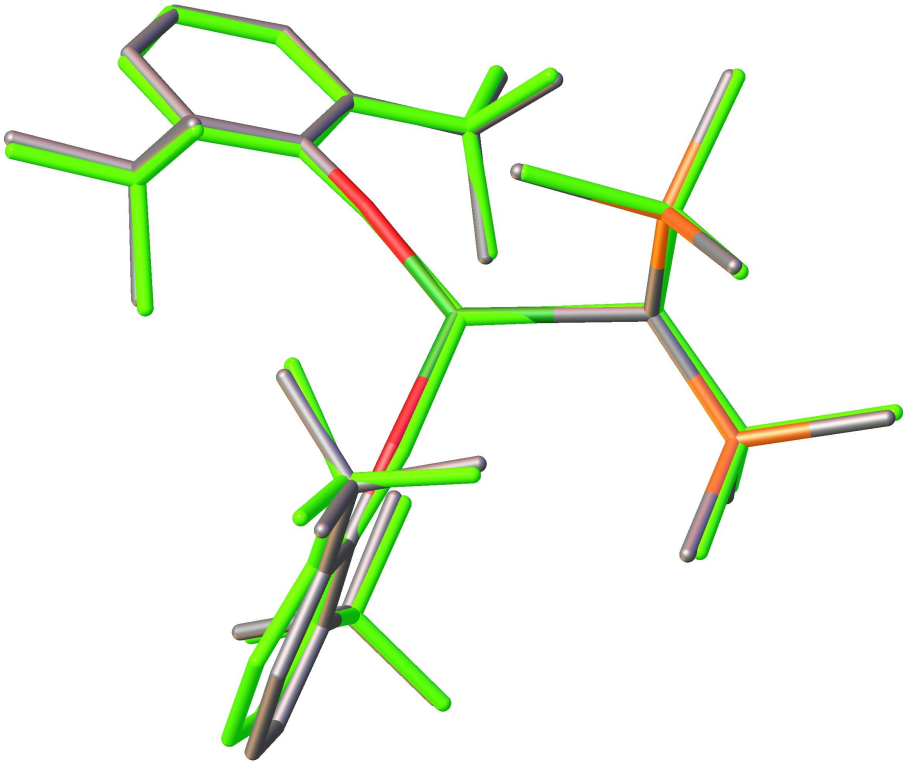

Figure S6: Overlay of both crystallographically independent molecules of Yb[CH(SiMe$_3$)$_2$][O−2,6−*t*Bu−C$_6$H$_3$]$_2$ in the asymmetric unit.

Table S6: Selected interatomic distances for Yb[CH(SiMe$_3$)$_2$][O−2,6−*t*Bu−C$_6$H$_3$]$_2$.

Atom 1	Atom 2	Distances in molecule A [Å]	Distances in molecule B [Å]
Yb1	Si2	3.069(2)	3.083(2)
Yb1	O1	2.033(5)	2.033(5)
Yb1	O2	2.012(5)	2.020(5)
Yb1	C1	2.352(7)	2.341(7)

3 Solution ^{1}H NMR experiments

The solution NMR of Yb[CH(SiMe$_3$)$_2$]$_3$ at 20°C consists of a single and rather broad ^{1}H resonance line at $\delta(^1\mathrm{H}) = 30$ ppm with $\nu_{1/2} = 1290$ Hz, as well as of the signals of the traces of CH$_2$(SiMe$_3$)$_2$ impurity at 0.01 ppm and −0.42 ppm (data not shown). This indicates that the SiMe$_3$ groups of Yb[CH(SiMe$_3$)$_2$]$_3$ are equivalent. Since the three SiMe$_3$ groups appear as three distinct resonances below −130°C for the isostructural diamagnetic Lu[CH(SiMe$_3$)$_2$]$_3$ complex,[46] the NMR studies of a solution of Yb[CH(SiMe$_3$)$_2$]$_3$ in per-deuterated methylbutane were carried out at different temperatures. It appeared that the single resonance line at $\delta(^1\mathrm{H}) = 30$ ppm broadens and shifts linearly downfield to $\delta(^1\mathrm{H}) = 32$ ppm with decreasing temperature down to T = 210 K. For lower temperatures, the slope of this dependency increases rapidly, while the signal broadens and completely disappears at approximately 190 K (Figure S7). No decoalescence of overlapping signals was observed, in contrast to what was found for Lu[CH(SiMe$_3$)$_2$]$_3$ complex.[46] The change in slope may be attributed to a change from rapid to slow exchange regime. The equal population two-site exchange process of the two TMS groups being the only conceivable physical process, one would expect a second branch with a negative slope. One possible explanation is that, at sufficiently low temperatures, the Yb···Cγ–Siβ interaction is observed in solution, resulting in a shortening of the T_2 of the protons, leading to unobservable resonances.

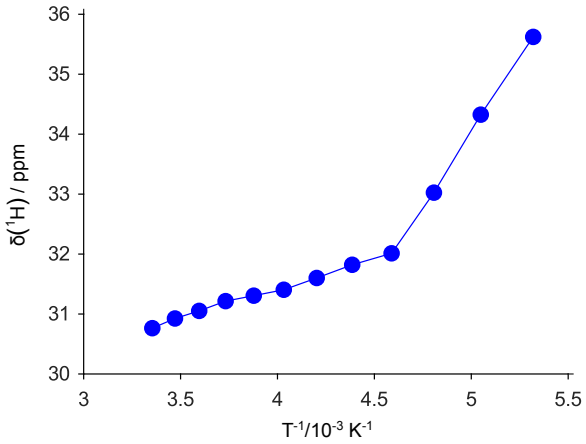

Figure S7: Dependence of a central position of a broad ^{1}H resonance line (400 MHz, deuterated isopentane) on T^{-1} for the $Yb[CH(SiMe_3)_2]_3$ complex.

4 EPR characterization

4.1 HYSCORE simulations

The experimental HYSCORE spectrum of $Yb[CH(SiMe_3)_2]_3$ (Figure 3) was measured at the field position indicated by the red arrow on the echo-detected EPR spectrum in Figure 3b of the main text. At this orientation, the ESEEM modulations in time-domain HYSCORE traces appeared to have maximal depth, leading to the best signal-to-noise ratio for the ^1H signals in ESEEM and HYSCORE spectra.

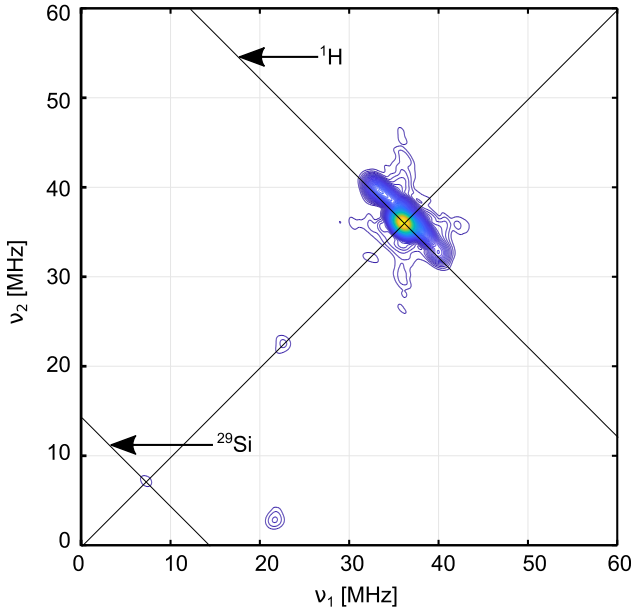

Figure S8: Experimental HYSCORE spectrum of $Yb[CH(SiMe_3)_2]_3$ (blue to yellow).

5 Computational modeling

5.1 DFT-optimized structure of $Yb[CH(SiMe_3)_2]_3$

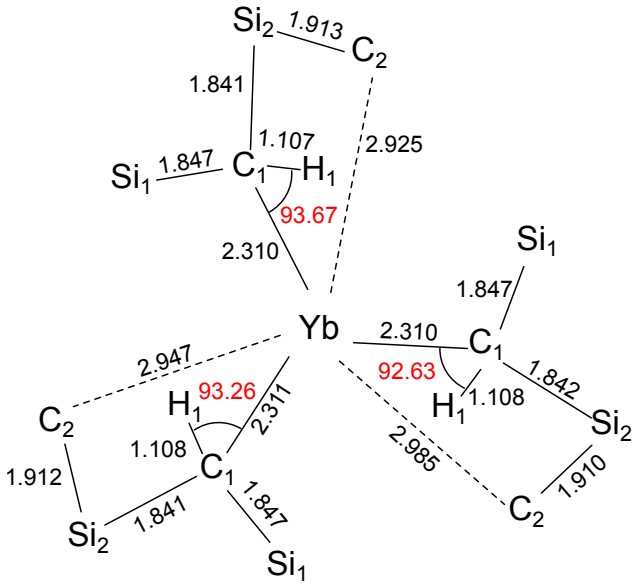

Figure S9: DFT optimized structure of $Yb[CH(SiMe_3)_2]_3$.

Table S7: Selected bond lengths and angles for one of the $CH(SiMe_3)_2$ ligands in the DFT-optimized structure of $Yb[CH(SiMe_3)_2]_3$.

Distances [Å]									
Yb–H(1)	Yb–C(1)	Yb–C(2)	Yb–Si(1)	Yb–Si(2)	Si(2)–C(1)	Si(2)–C(2)	Si(2)–C(3)	Si(1)–C(1)	Si(1)–C(5)
2.619	2.311	2.947	3.716	3.232	1.841	1.912	1.875	1.847	1.879
2.625	2.310	2.925	3.716	3.219	1.841	1.913	1.875	1.847	1.879
2.607	2.310	2.985	3.711	3.251	1.842	1.910	1.875	1.847	1.880

Angle [°]						
Yb–C(1)–H(1)	Yb–C(1)–Si(1)	Yb–C(1)–Si(2)	Yb–C(2)–Si(2)	Yb–C(1)–C(2)	C(1)–Si(2)–C(2)	C(1)–Yb(1)–C(1′)
93.26	126.36	101.63	80.32	65.56	107.13	108.57
93.67	126.43	101.09	80.46	65.02	106.97	108.72
92.63	126.09	102.51	79.97	66.59	107.17	108.55

Table S8: Cartesian coordinates of the DFT-optimized structure of $Yb[CH(SiMe_3)_2]_3$. Labels of the atomic positions were kept in accordance with Fig. 2b-c of the main text.

Element	x [Å]	y [Å]	z [Å]	Element	x [Å]	y [Å]	z [Å]
Yb	8.101	4.659	6.915	H_6	3.293	2.133	8.364
Si_2	5.968	2.326	6.243	H_6	3.037	2.855	9.954
Si_1	5.007	3.899	8.829	H_6	4.331	1.673	9.717
Si_2	11.186	4.014	6.265	H_5	6.226	3.734	10.996
Si_1	10.307	2.365	8.834	H_5	4.914	4.909	11.100
Si_2	7.114	7.679	6.227	H_5	6.428	5.340	10.297
Si_1	8.964	7.733	8.808	H_3	6.711	0.066	7.006
C_1	6.376	3.348	7.719	H_3	5.585	-0.059	5.649
C_6	3.804	2.513	9.253	H_3	4.984	0.307	7.273
C_5	5.710	4.530	10.453	H_4	3.533	2.746	5.937
C_2	7.410	2.526	5.003	H_4	4.301	2.281	4.418
C_3	5.802	0.488	6.571	H_4	4.467	3.930	5.022
C_4	4.428	2.881	5.324	H_7	4.635	6.168	7.872
C_7	4.011	5.290	8.048	H_7	3.196	5.593	8.711
C_1	10.096	3.836	7.738	H_7	3.569	4.995	7.094
C_6	12.110	2.016	9.254	H_2	7.297	1.825	4.172
C_5	9.408	2.643	10.460	H_2	8.389	2.306	5.448
C_2	10.285	5.175	5.040	H_2	7.440	3.516	4.524
C_3	12.860	4.787	6.604	H_1	7.053	2.726	8.337
C_4	11.478	2.415	5.325	H_6	12.694	1.775	8.361
C_7	9.606	0.814	8.035	H_6	12.199	1.172	9.945
C_1	7.810	6.814	7.696	H_6	12.572	2.886	9.727
C_6	8.356	9.466	9.229	H_5	9.833	3.490	11.006
C_5	9.162	6.816	10.436	H_5	9.486	1.763	11.104
C_2	6.544	6.334	4.997	H_5	8.347	2.851	10.306
C_3	5.616	8.751	6.577	H_3	12.772	5.775	7.060
C_4	8.361	8.731	5.297	H_3	13.440	4.892	5.683
C_7	10.665	7.910	8.027	H_3	13.428	4.154	7.291
				H_4	12.047	1.702	5.926
				H_4	12.056	2.618	4.419
				H_4	10.550	1.926	5.021
				H_7	8.533	0.914	7.859
				H_7	9.752	-0.052	8.687
				H_7	10.085	0.593	7.079
				H_2	10.955	5.459	4.224
				H_2	9.963	6.118	5.502
				H_2	9.428	4.702	4.538
				H_1	10.288	4.729	8.364
				H_6	8.282	10.097	8.339
				H_6	9.033	9.961	9.931
				H_6	7.366	9.426	9.691
				H_5	8.215	6.770	10.981
				H_5	9.888	7.321	11.079
				H_5	9.505	5.789	10.288
				H_3	4.798	8.178	7.021
				H_3	5.241	9.217	5.661
				H_3	5.881	9.547	7.278
				H_4	8.701	9.571	5.906
				H_4	7.897	9.144	4.396
				H_4	9.243	8.168	4.985
				H_7	11.124	6.933	7.862
				H_7	11.329	8.479	8.683
				H_7	10.623	8.428	7.066
				H_2	5.972	6.781	4.179
				H_2	5.877	5.595	5.460
				H_2	7.376	5.814	4.501
				H_1	6.937	6.526	8.314

5.2 NBO analysis

The degree of π character in Yb-C bonds was estimated in a Natural Hybrid Orbital (NHO) Directionality and Bond Bending analysis, available in the NBO program.[38] The provided NHO deviation angles are the angles between the internuclear vector (i.e. Yb-C vector) and the direction of the NHO orbital, determined numerically to correspond to maximum angular amplitude. For a pure σ-bond, such an angle would correspond to 0°, while pure π-type orientation corresponds to 90°. Thus, increasing values of NHO deviation are associated with increasing mixing with orbitals that are not along the Yb-C bond, being an indication of the partial π character.[47,48] In particular, such method was used to estimate the partial π character in the metal-carbon bonds for the neutral molecular complexes $Cp_2TiEtCl$, $Cp_2ZrEtCl$ (NHO deviation 5.7 ° for both complexes)[47] and Ti(nacnac)(CH_2^tBu)$_2$ (NHO deviations 15.0° and 14.4° for the two Ti-C bonds). The obtained NHO deviations for the Yb-C bonds of Yb[$CH(SiMe_3)_2$]$_3$ (17.8°, 17.9° and 17.9°, respectively) point towards the presence of stronger π character within these bonds. At the same time, for the calculated structures of cationic complexes the deviation values are usually higher, lying typically between 20° and 30°. As the unrestricted NBO analysis was performed, two sets of natural orbitals were obtained for all studied structures, related to spin-α and spin-β molecular orbitals; the maximal occupation of each natural orbital appeared equal to 1. The NBO analysis revealed two sets of five natural orbitals of d character, having lowest energies among all the natural orbitals with low occupancies, which are not corresponding to antibonding natural orbitals related to the chemical bonds of Yb[$CH(SiMe_3)_2$]$_3$. Their energies, occupancies, and stabilization energies, calculated via the "deletion" procedure[38] and referred to as a sum of contributions from all the secondary (donor-acceptor) interactions that involve the selected orbital, are summarized in Table S9. For simplicity, and since these values are rather similar for both spin-α and spin-β natural orbitals, only the values for the spin-α orbitals are shown.

Table S9: Spin-α natural orbitals, related to the 5d orbitals of Yb in $Yb[CH(SiMe_3)_2]_3$.

Number	Energy [Hartree]	Occupancy (out of 1)	Stabilization energy [kcal/mol]
170	0.20809	0.05836	44.284
171	0.20567	0.05760	38.595
172	0.13851	0.05079	39.342
257	0.42100	0.04040	44.255
258	0.42228	0.03939	25.212

All the five obtained natural orbitals have relatively high occupancies; in fact, occupancies of all natural orbitals with the numbers higher than 258 are smaller than 0.004. This allows us to assign the natural orbitals listed in Table S9 to the 5d orbitals of Yb in $Yb[CH(SiMe_3)_2]_3$. Among them, the first three orbitals (170 - 172) have the lowest energies among all natural orbitals with low occupancies, including the antibonding orbitals of $Yb[CH(SiMe_3)_2]_3$, and a significant energy splitting between them and another two 5d orbitals is observed. Also, their occupancies are all higher than 0.05, while that is not the case for the two high-energy orbitals. Therefore, it is likely that these three low-lying orbitals are involved in the secondary interactions, including α-H agostic interactions that bring the π character to the Yb-C bonds, and the three-center - two-electron Yb-Me-Si interactions. Indeed, for one of these orbitals (number 171), both interactions were visualized on Fig. 4 of the main text.

5.3 Prediction of paramagnetic shifts

The distribution of ^{1}H shifts displayed in Fig. 5 was calculated following the formalism of Moon and Patchkovski[49] in the implementation developed by Vaara et al.[50–52] and van den Heuvel and Soncini.[53,54] The total NMR shielding can be expressed as

$$\sigma = \sigma_{\text{orb}} + \sigma_{\text{epr}} \tag{5}$$

$$\sigma_{\text{epr}} = -\frac{\mu_B}{\hbar\gamma_I k_B T}\mathbf{g}\cdot\langle\mathbf{SS}\rangle\cdot\mathbf{A}, \tag{6}$$

where k_B, μ_B, γ_I, T are the Boltzmann constant, Bohr magneton, gyromagnetic ratio of the nucleus and absolute temperature, respectively. σ_{orb} corresponds to the diamagnetic contribution to the NMR shielding, as defined by Ramsey,[55,56] $\mathbf{g}$ corresponds to the g tensor and the term $\langle\mathbf{SS}\rangle$ is the spin dyadic tensor given by:

$$\langle S_a S_b\rangle = \frac{\sum_{nm} Q_{nm}\langle n|S_a|m\rangle\langle m|S_b|n\rangle}{\sum_n \exp\left(-\frac{-E_n}{k_B T}\right)}, \quad a,\, b{=}\{x,y,z\} \tag{7}$$

$$Q_{nm} = \begin{cases} \exp\left(-\frac{E_n}{k_B T}\right), & E_n = E_m \\ -\frac{k_B T}{E_m - E_n}\left[\exp\left(-\frac{E_m}{k_B T} - \frac{E_n}{k_B T}\right)\right], & E_n \neq E_m \end{cases} \tag{8}$$

where $S_{a,b}$ are components of the effective spin operator and E_n is the energy of the state $|n\rangle$ at the zero magnetic field. This equation can be further simplified to

$$\sigma_{\text{epr}} = -\frac{\mu_B}{4\hbar\gamma_I k_B T}\mathbf{g}\cdot\mathbf{A}, \tag{9}$$

for a system with effective spin $S = 1/2$ and, hence, in the absence of zero-field splitting.

Long-range effects from neighboring unit cells are calculated considering a semi-empirical

point-dipole approximation[57]

$$\sigma_{\mathrm{pcs,lr}} \approx -\frac{1}{4\pi r^3}\chi\left(\frac{3\mathbf{r}\otimes\mathbf{r}^T}{r^2}-\mathbb{I}\right), \tag{10}$$

where χ is calculated at 300 K according to the SO-CASPT2 method and $\mathbf{r}$ is the distance between the NMR nucleus and the paramagnetic center and $\mathbb{I}$ is the identity matrix.

The NMR shielding tensors (σ) were converted to shift convention according to

$$\delta = \sigma_{\mathrm{ref}} - \sigma, \tag{11}$$

where

$$\sigma_{\mathrm{ref}} = \sigma_{\mathrm{calc}} - \sigma_{\mathrm{exp}}, \tag{12}$$

σ_{exp} and σ_{calc} correspond to the experimental and calculated isotropic shielding of a chosen reference compound, namely tetramethylsilane (TMS).

Table S10: Calculated and experimental SA parameters for the proximal (denoted by p) and distal (denoted by d) $-SiMe_3$ groups of $Yb^{III}(CH(SiMe_3)_2)_3$ complex in the Haeberlen convention before a 3-site fast exchange averaging of the shielding tensors. The shielding tensor is computed according to eq. 2, where the magnetic susceptibility tensor has been computed with SO-CASPT2 method and the hyperfine tensors are either from the SO-CASSCF or DFT(PBE0) method. Long-range contributions were accounted for using the semi-classical point dipolar equation according to eq. SI 10.

Method		^{29}Si		^{13}C			^{1}H				
		p	d	$p^{(ag)}$	p	p	d	$p^{(ag)}$	p	p	d
SO-CASPT2/CASSCF	δ^{orb}	-10.7	-9.2	4.8	4.3	-0.7	4.6	0.7	0.1	-0.2	0.4
	δ^{LR}	16.9	16.5	15.9	72.6	-3.1	9.5	17.2	12.7	17.0	27.7
	δ^{SD}	-67.3	-9.6	28.5	-18.3	-23.5	0.5	51.8	-17.6	-12.0	2.1
	δ^{PSO}	-200.9	-29.2	76.8	-55.1	-69.6	1.7	152.9	-52.5	-36.2	6.6
	δ^{FC}	2.8	7.6	6.6	-19.1	19.9	0.5	0.8	0.0	-0.1	0.0
	δ^{total}	-259.2	-23.9	132.6	-15.6	-77.0	16.8	223.4	-35.8	-53.0	36.8
	$\Delta\delta$	-493.2	-19.3	-350.0	-18.5	-30.2	-28.4	82.8	81.5	149.0	21.8
SO-CASPT2/PBE0	δ^{SD}	-61.2	-10.2	36.9	-23.4	-16.3	-0.4	45.3	-15.6	-10.8	1.9
	δ^{PSO}	-78.4	-10.3	22.3	-23.4	-24.7	1.0	56.4	-19.5	-14.8	2.4
	δ^{FC}	-24.4	-77.4	173.3	31.1	-1.5	14.7	8.6	-0.3	-0.1	0.4
	δ^{total}	-157.8	-90.6	253.2	61.2	-46.3	29.4	128.2	-68.2	-83.8	34.7
	$\Delta\delta$	-321.8	-122.0	-684.5	-88.3	-4.5	-51.0	106.6	31.6	62.8	18.3
Exp	δ	-220±20	-30±30	40±20		-20±20		30±20		-20±20	
	$\Delta\delta$	-542±3	409±3	-183±4		140[+30,-270]		153±1		-56±1	

5.4 Modeling molecular dynamics from NMR data

In solution, the ^{1}H NMR spectrum contains a single broad signal. Between ≈182 K and ≈222 K the measured shift varies from 36 ppm to 32 ppm, following a typical Curie behavior. At ≈222 K, there is a reduction in the slope and further heating to 285 K results only in a shift decrease by a further 1 ppm (see Figure S7). Throughout this temperature range, only the ground KD is significant populated, so this change in temperature dependence of the shifts is not attributable to population of the excited states, but rather indicates the onset of dynamical processes at ≈222 K.

Interestingly, at no points can we resolve the individual signals in the slow exchange regime, likely due to the high degree of broadening from paramagnetic effects, in contrast to the diamagnetic Lu complex.[46] For the Lu complex, it was proposed that the silicon sites are undergoing a rapid site exchange in solution resulting in an averaged out signal for the $-SiMe_3$ protons.

To check that this hypothesis also applies to the Yb complex, the energy barrier was estimated for rotation of the proximal $-SiMe_3$ group about the $C_\alpha - Si$ bond, with subsequent geometry optimization of the dynamical intermediates in the gas phase. It was observed that, due to disruption of the $Yb - C_\gamma$ agostic interaction upon this rotation, the entire molecule rearranges itself from the out-of-plane (XRD) geometry to an in-plane configuration, where Yb center is moved towards the plane defined by the three coordinating C_α atoms. In concert with this distortion, the two methyl groups (previously designated proximal and distal) are now chemically equivalent, and become agostically bonded (see Figure S10). Further disruption is caused by the rotation of these agostically bonded methyl groups in this intermediate in-plane $Yb^{III}(CH(SiMe_3)_2)_3$ complex, which relaxes the geometry to an out-of-plane structure. DFT-based geometry optimizations suggest that this process, and the required energy, are governed by the molecular rearrangement required to maintain agostic interactions. The rotational energy barrier was calculated to have an upper bound of 16 kJ/mol at

the ZORA-DFT(PBE0) level, which is greater than the thermal energy at room temperature (≈2.4 kJ/mol). Nevertheless, we have not sampled the full energy landscape of the complex, and so the true activation energy for this process is likely to be significantly lower. This dynamical process renders all the methyl protons chemically equivalent, as observed in the solution NMR spectrum.

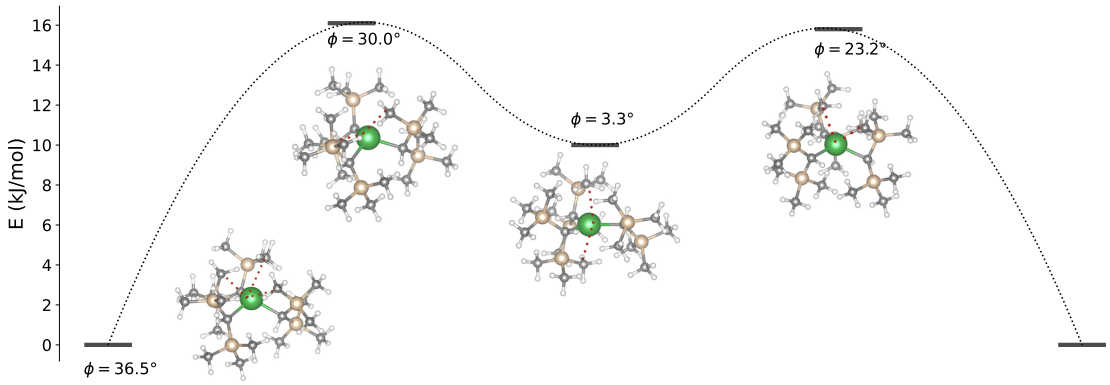

Figure S10: ZORA-DFT(PBE0) based energy profile of the site exchange process of the $-SiMe_3$ groups. The dynamical structures are also shown with the agostic interactions (marked by dotted lines). The out-of-plane angles ϕ show the movement of the central ion in and out of the plane of the three coordinating C_α atoms during the profile.

Unsurprisingly, this complete averaging process is hindered in the solid state, to the extent that we still see distinct signals from the proximal and distal moieties. It is however interesting that the residual dynamics described earlier still persists within the constraints posed by the lattice.

6 Magnetic susceptibility studies

The solid-state magnetic susceptibility of three complexes $Yb[CH(SiMe_3)_2]_x[O{-}2,6{-}t BuC_6H_3]_{3-x}$ ($x = 1$, 2, 3), together with the starting material $Yb[CH(SiMe_3)_2]_3$ ($x = 0$), was measured as a function of temperature between 2.6 and 300 K using an applied magnetic field of 1 kOe. Figure S11 shows the results for $Yb[CH(SiMe_3)_2]_3$, whereas data for the other ytterbium compounds are provided in Figures S12 - S14.

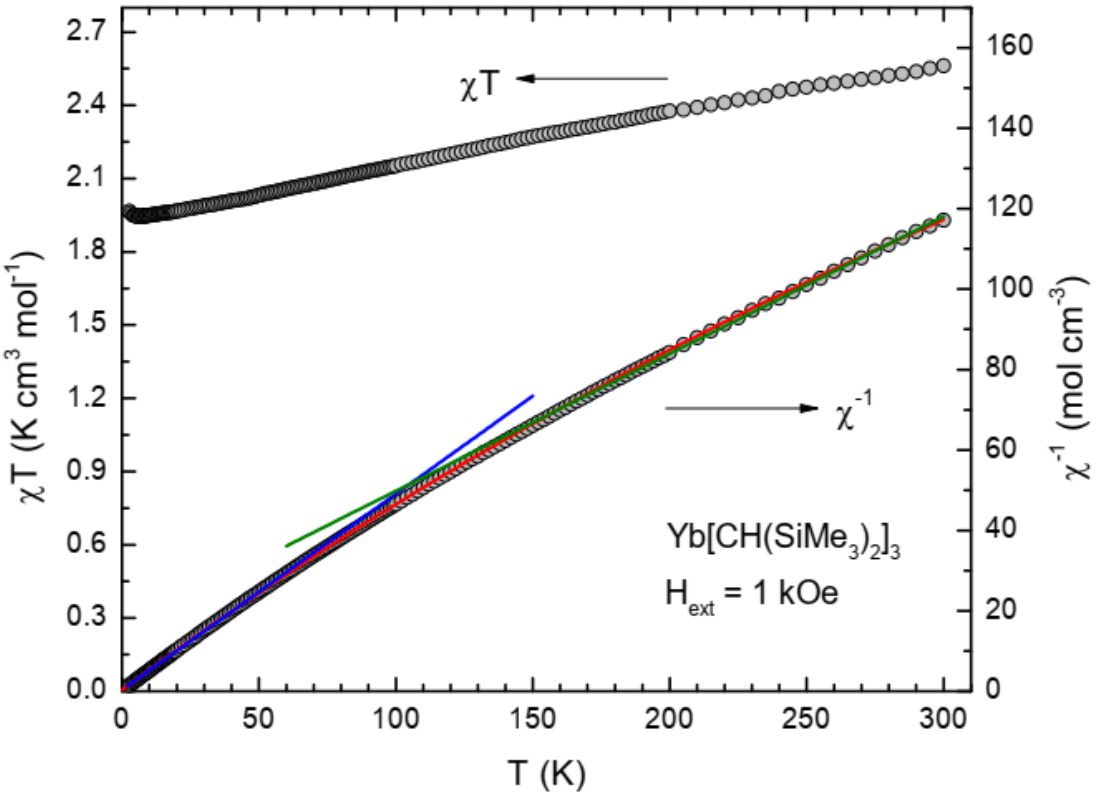

Figure S11: Magnetic susceptibility (χT) and inverse magnetic susceptibility (χ^{-1}) versus temperature (T) of complex $Yb[CH(SiMe_3)_2]_3$. Symbols: Experimental data. Lines: (Red) fit with a Curie-Weiss-law approximation, modified by a phenomenological temperature-independent (TIP) contribution; (Blue) fit of the data with T $<$ 60 K and fixed $\chi_{TIP} = 0$; (Green) fit of the data with T $>$ 150 K and fixed $\chi_{TIP} = 0$. The parameters of the fits are summarized in Table S11.

All four ytterbium complexes exhibit experimental values for the effective magnetic mo-

ment at 300 K that are in the range between μ_{eff}(300 K)= 4.30 μ_B (χT = 2.31 cm^3 K mol^{-1}) and 4.53 μ_B (χT = 2.57 cm^3 K mol^{-1}), respectively. These values are in good agreement with those from the electronic configuration of the free Yb(III) ion, which is described by a single $^2F_{7/2}$ term, for which μ_{eff} = 4.54 μ_B (χT = 2.58 cm^3 K mol^{-1}) is expected. Although all the ytterbium complexes studied in this work can be well-described as Yb(III), $4f^{13}$ systems, the origin of the small variations in their $\mu_{\text{eff}}^{(300\text{K})}$ values cannot be unambiguously explained. Several factors may contribute such as small deviations in the orbital reduction factor,[58] or small changes in the crystal field splitting pattern for the individual ytterbium complexes (also affecting the degree of admixture of excited crystal field multiplets into the ground state, causing a temperature-independent (TIP) contribution to the magnetic susceptibility[59]), as a consequence of the different substituents in the investigated series.

The χT values of the starting material also exhibit a slight temperature dependence, as they decrease to approx. μ_{eff} = 4.0 μ_B (χT = 2.00 cm^3 K mol^{-1}) at 2.6 K. Such a temperature dependence is generally rationalized by the change in population of the closely separated crystal field states of the individual molecules. Very detailed ligand field analyses are unfortunately only available for Yb(III) compounds with high molecular symmetry, for which a marked temperature dependence in the effective magnetic moment was observed[60,61] whereas for complexes with lower coordination number and molecular symmetry no detailed analysis and only limited experimental data are available. For instance, similar small variations in the effective magnetic moments as a function of temperature were previously observed for a series of organometallic ytterbium complexes.[62] However, in the absence of additional data we refrain from a more detailed analysis.

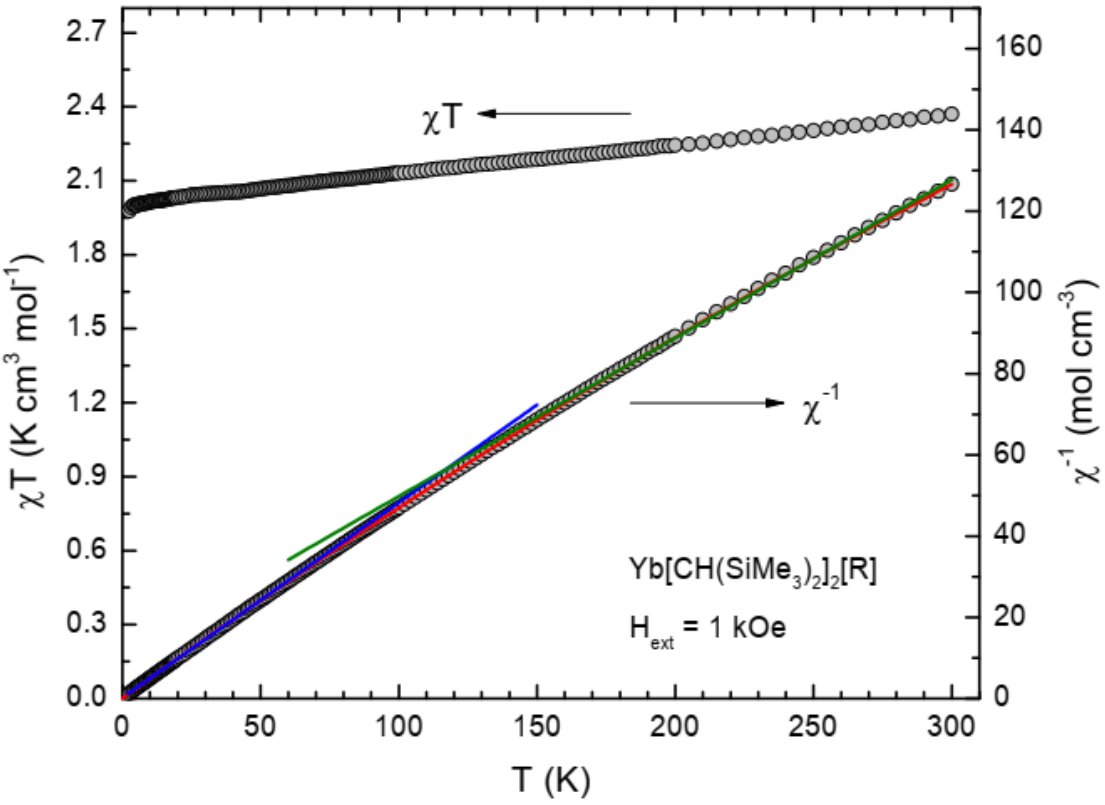

Figure S12: Magnetic susceptibility (χT) and inverse magnetic susceptibility (χ^{-1}) versus temperature (T) of complex Yb[CH(SiMe$_3$)$_2$]$_2$[R] (R = O−2,6−tBu$_2$−C$_6$H$_3$). Symbols: Experimental data. Lines: (Red) fit with a Curie-Weiss-law approximation, modified by a phenomenological temperature-independent (TIP) contribution; (Blue) fit of the data with T $<$ 60 K and fixed $\chi_{TIP} = 0$; (Green) fit of the data with T $>$ 15K and fixed $\chi_{TIP} = 0$. The parameters of the fits are summarized in Table S11.

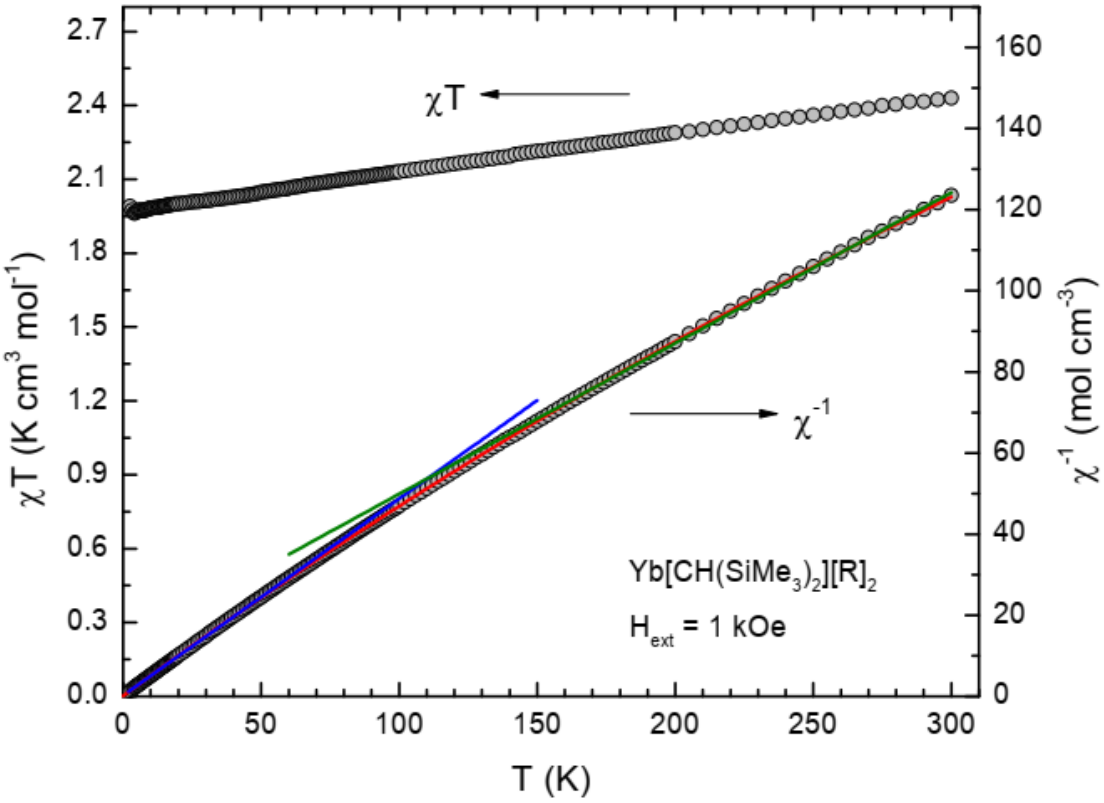

Figure S13: Magnetic susceptibility (χT) and inverse magnetic susceptibility (χ^{-1}) versus temperature (T) of complex Yb[CH(SiMe$_3$)$_2$][R]$_2$ (R = O−2,6−tBu$_2$−C$_6$H$_3$). Symbols: Experimental data. Lines: (Red) fit with a Curie-Weiss-law approximation, modified by a phenomenological temperature-independent (TIP) contribution; (Blue) fit of the data with T $<$ 60 K and fixed $\chi_{TIP} = 0$; (Green) fit of the data with T $>$ 15K and fixed $\chi_{TIP} = 0$. The parameters of the fits are summarized in Table S11.

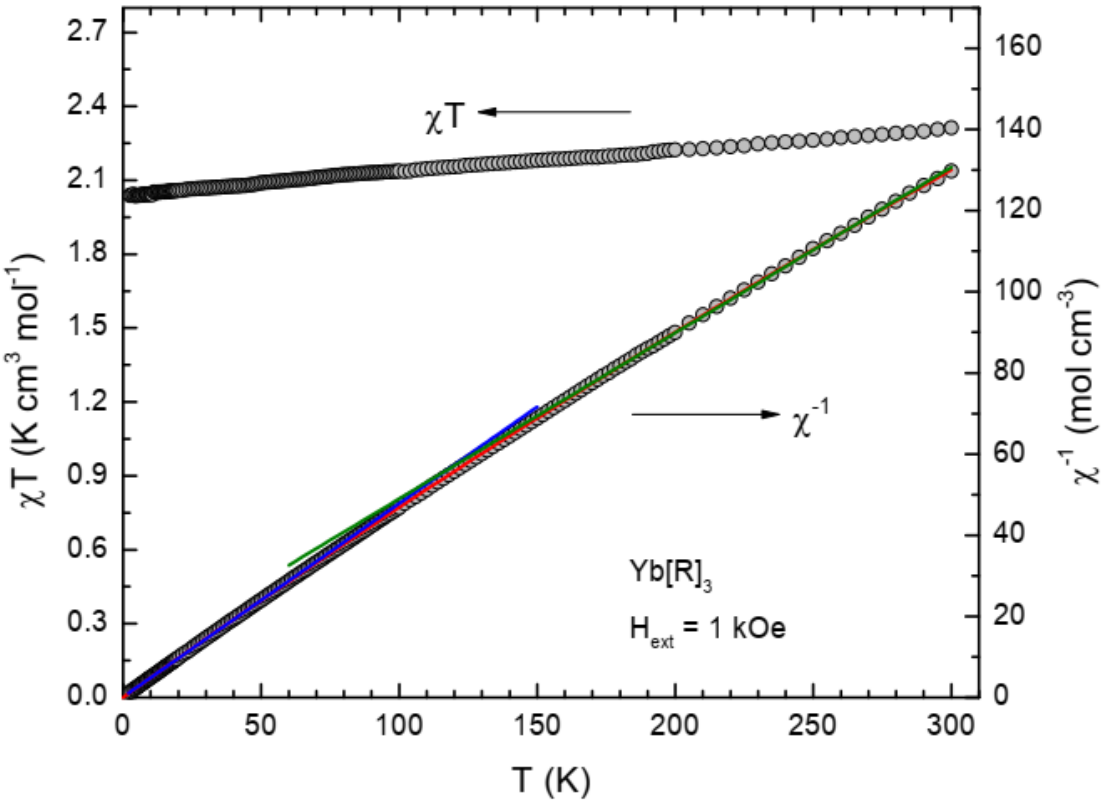

Figure S14: Magnetic susceptibility (χT) and inverse magnetic susceptibility (χ^{-1}) versus temperature (T) of complex Yb[R]$_3$ (R = O$-$2,6$-t$Bu$_2-$C$_6$H$_3$). Symbols: Experimental data. Lines: (Red) fit with a Curie-Weiss-law approximation, modified by a phenomenological temperature-independent (TIP) contribution; (Blue) fit of the data with T $<$ 60 K and fixed $\chi_{TIP} = 0$; (Green) fit of the data with T $>$ 15K and fixed $\chi_{TIP} = 0$. The parameters of the fits are summarized in Table S11.

Table S11: Effective magnetic moment at 300 and 2.6 K of $Yb[CH(SiMe_3)_2]_{3-x}$[O-2,6-tBu$_2$-$C_6H_3]_x$ with x = 0, 1, 2, 3 and parameters of three different fits based on the Curie-Weiss-law approximation. The restrictions used for the individual fit strategies are given in the last column of the table.[a]

	$Yb[L]_3$	$Yb[L_2]R$	$Yb[L][R]_2$	$Yb[R]_3$	
$\mu_{\text{eff}}^{300K}/\mu_{\text{eff}}^{2.6K}(\mu_B)$	4.53/3.97	4.35/3.98	4.41/3.99	4.30/4.04	
C(cm^3 mol^{-1} K)	1.961(3)	2.009(1)	1.987(1)	2.052(1)	T < 300 K
$\mu_{\text{eff}}(\mu_B)$	3.96	4.01	3.99	4.05	T < 300 K
θ (K)	-0.48(7)	0.00(<1)	-0.23(3)	-0.09(2)	T < 300 K
χ_{TIP}(cm^3 mol^{-1})	20(1)×10^{-4}	12(1)×10^{-4}	15(<1)×10^{-4}	8.5(1)×10^{-4}	T < 300 K
C(cm^3 mol^{-1} K)	2.052(4)	2.080(2)	2.062(3)	2.098(2)	T < 60 K
$\mu_{\text{eff}}(\mu_B)$	4.05	4.08	4.06	4.10	T < 60 K
θ (K)	-0.64(6)	-0.37(3)	-0.48(4)	-0.30(3)	T < 60 K
χ_{TIP}(cm^3 mol^{-1})	-*	-*	-*	-*	T < 60 K
C(cm^3 mol^{-1} K)	2.929(11)	2.565(10)	2.690(9)	2.446(6)	T > 150 K
$\mu_{\text{eff}}(\mu_B)$	4.84	4.53	4.64	4.42	T > 150 K
θ (K)	-45.8(1.0)	-27.7(9)	-34.2(8)	-19.8(6)	T > 150 K
χ_{TIP}(cm^3 mol^{-1})	-*	-*	-*	-*	T > 150 K

L = $CH(SiMe_3)_2$; R = O-2,6-tBu$_2$-C_6H_3; [*] Fixed in the fit. [**a**] Two different fit strategies were followed: (A) Fitting of the inverse magnetic susceptibility (χ^{-1}) vs. temperature (T) using a Curie-Weiss law approximation, modified by a phenomenological temperature-independent (TIP) contribution. (B and C) Separation of the (χ^{-1}) vs. T fits into two different temperature regimes (i.e., T < 60 K and T > 150 K) assuming that at low temperature only the lowest M_J state(s) is (are) occupied, whereas with increasing temperature also the other states become populated. A similar approach was previously reported, e.g. by Schulz et al.[63] .

7 NMR characterization of $\mathbf{Yb[CH(SiMe_3)_2]_{3-x}[O{-}2,6{-}}t\mathbf{Bu_2{-}C_6H_3]_x}$ ($x = 1, 2$) complexes

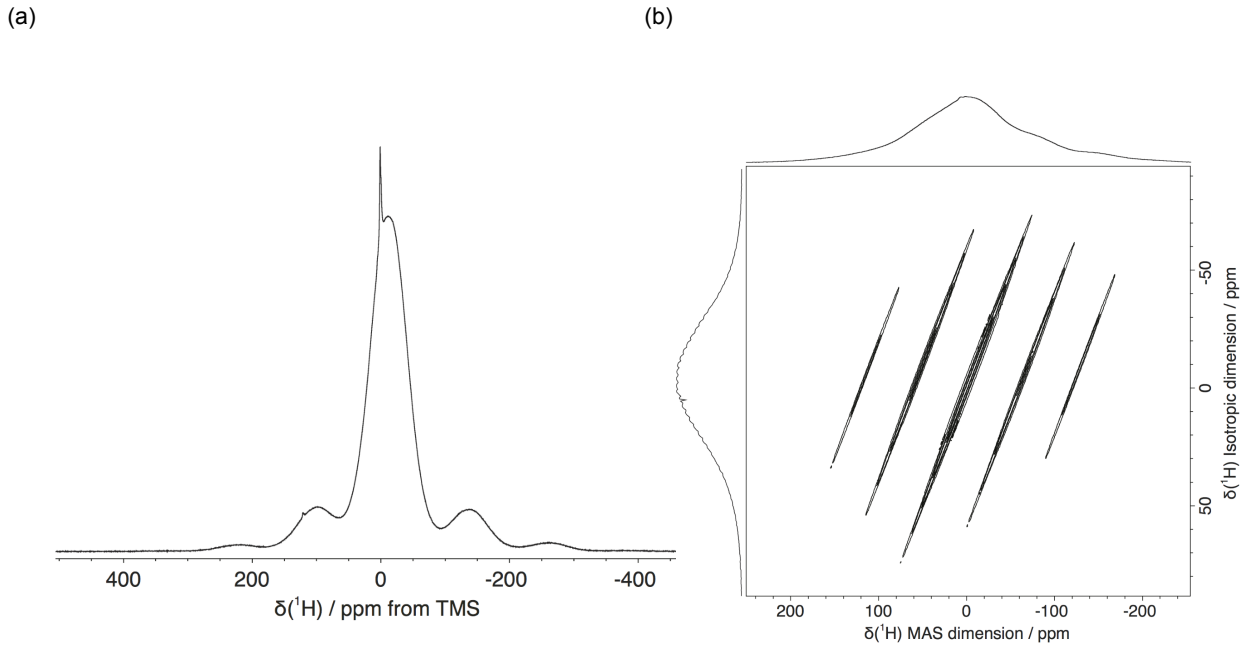

Figure S15: (a) ^{1}H NMR spectrum (500 MHz, Bruker HX 1.3 mm probe, spinning rate 60 kHz, RF field strength of $\nu_{1,max}$= 319 kHz and 10 ms recycle delay) of [O−2,6−tBu−C_6H_3]Yb[$CH(SiMe_3)_2$]$_2$. (b) ^{1}H aMAT spectrum (500 MHz, spinning rate 31.25 kHz, RF field strength of $\nu_{1,max}$= 122 kHz and 10 ms recycle delay) of [O−2,6−tBu−C_6H_3]Yb[$CH(SiMe_3)_2$]$_2$.

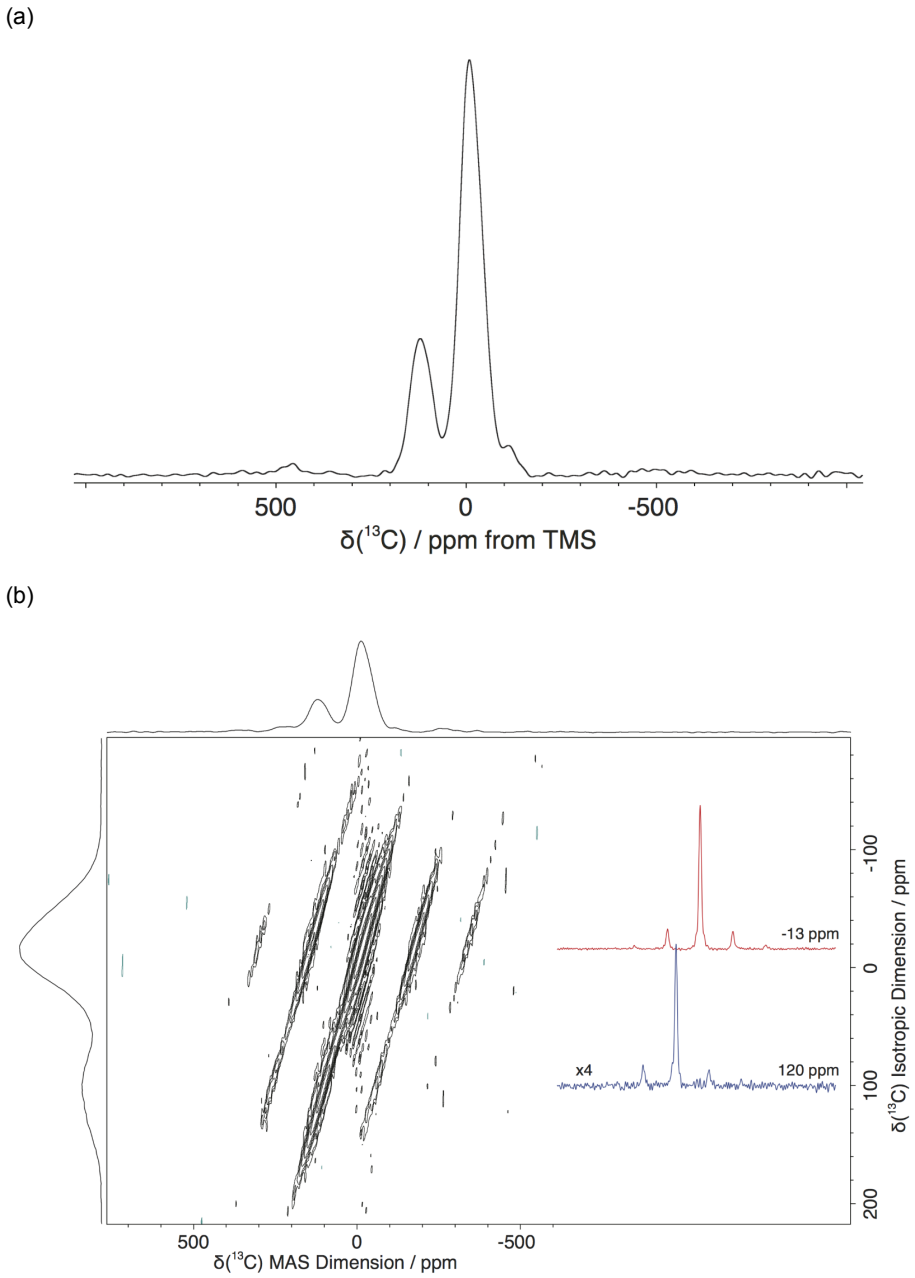

Figure S16: (a) ^{13}C NMR spectrum (500 MHz, Bruker HX 1.3 mm probe, spinning rate 60 kHz RF field strength of $\nu_{1,max}$= 189 kHz and 10 ms recycle delay) of [O−2,6−*t*Bu−C_6H_3]Yb[$CH(SiMe_3)_2$]$_2$. Two features are observed at −13 ppm and 120 ppm. (b) ^{13}C aMAT spectrum (500 MHz, spinning rate 20 kHz , RF field strength of $\nu_{1,max}$= 100 kHz and 6.9 ms recycle delay) of [O−2,6−tBu−C_6H_3]Yb[$CH(SiMe_3)_2$]$_2$. Selected anisotropic cross sections are shown at their respective isotropic positions with respect to the 2D spectrum.

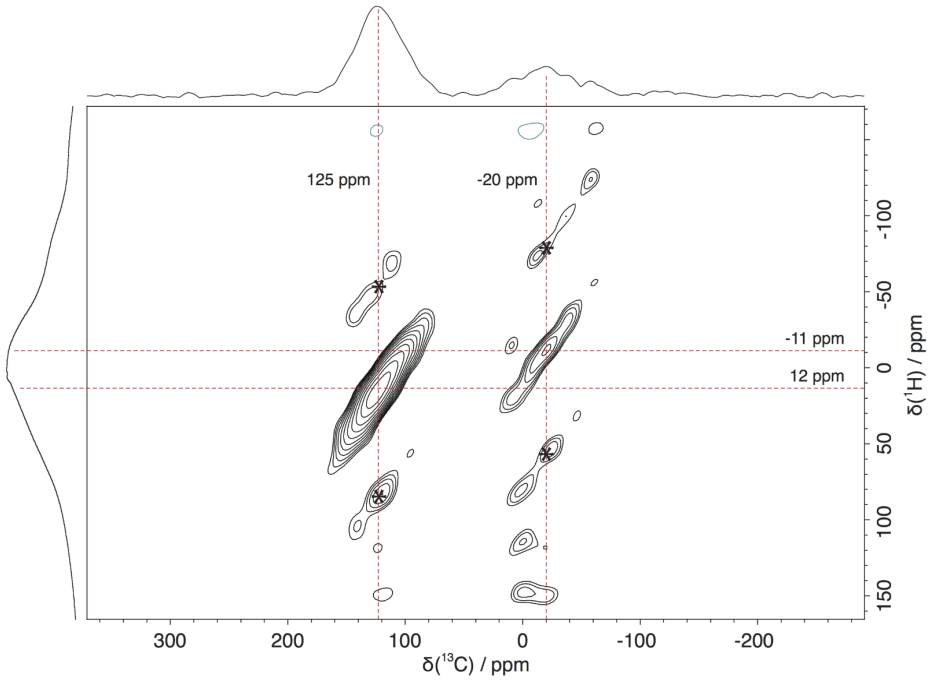

Figure S17: ^{1}H-^{13}C TEDOR NMR spectrum (500 MHz, spinning rate 31.25 kHz, RF field strength of $\nu_{1,max}$= 119 kHz and $\nu_{1,max}$= 202 kHz for ^{1}H and ^{13}C, respectively and 5 ms recycle delay) of [O−2,6−*t*Bu−C_6H_3]Yb[$CH(SiMe_3)_2$]$_2$. 131072 scans per increment and 120 t_1 increments were used with an increment of 5.00 μs for the delay.

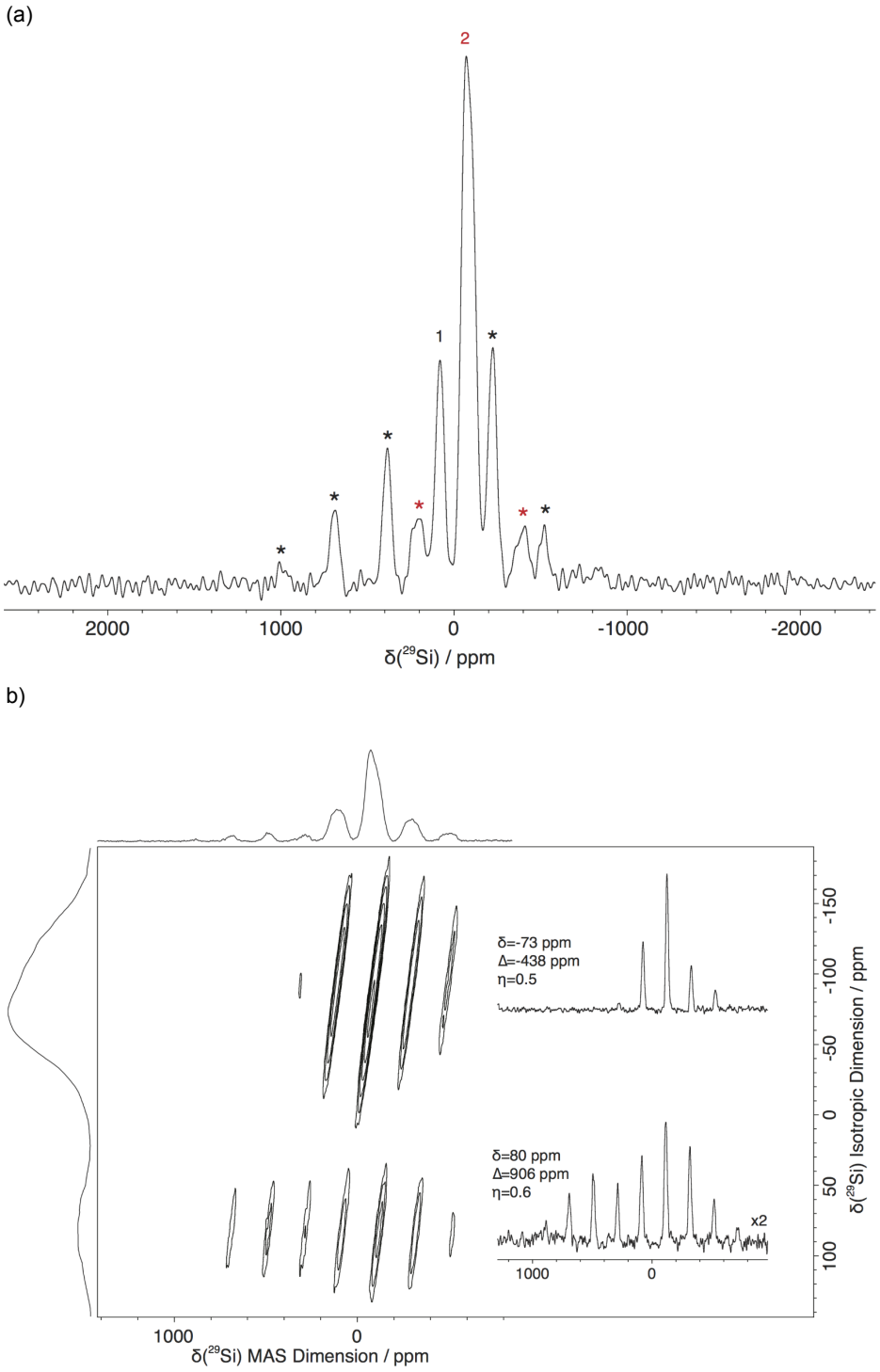

Figure S18: (a) ^{29}Si NMR spectrum (500 MHz, spinning rate 30 kHz, RF field strength of $\nu_{1,max}$= 118 kHz and 15 ms recycle delay) of [O−2,6−tBu−C_6H_3]Yb[$CH(SiMe_3)_2$]$_2$. Sidebands are marked with asterisks. (b) ^{29}Si aMAT spectrum (500 MHz, spinning rate 20 kHz, RF field strength of $\nu_{1,max}$= 118 kHz and 10 ms recycle delay) of [O−2,6−tBu−C_6H_3]Yb[$CH(SiMe_3)_2$]$_2$. Selected anisotropic cross sections are shown at their respective isotropic positions with corresponding CSA information provided in the inset.

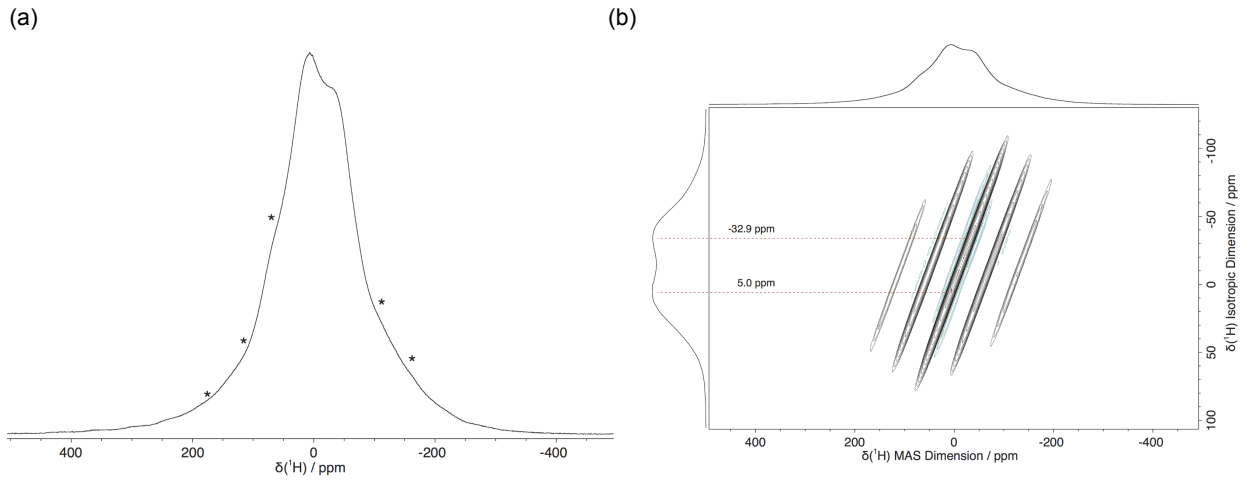

Figure S19: (a) ^{1}H NMR spectrum (500 MHz, spinning rate 30 kHz, RF field strength of $\nu_{1,max}$= 155 kHz and 2 ms recycle delay) of [O−2,6−tBu−C_6H_3]$_2$Yb[CH($SiMe_3$)$_2$]. Sidebands are marked with asterisks. (b) ^{1}H aMAT spectrum (500 MHz, spinning rate 30 kHz, RF field strength of $\nu_{1,max}$= 155 kHz and 2 ms recycle delay) of O−2,6−tBu−C_6H_3]$_2$Yb[CH($SiMe_3$)$_2$].

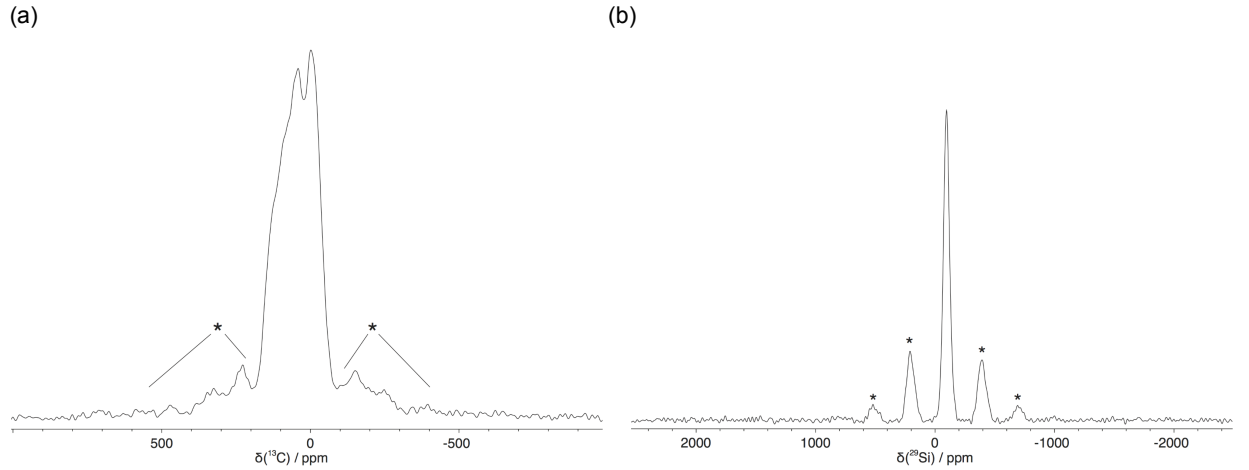

Figure S20: (a) ^{13}C NMR spectrum (500 MHz, spinning rate 30 kHz, RF field strength of $\nu_{1,max}$= 100 kHz and 4 ms recycle delay) of [O−2,6−tBu−C_6H_3]$_2$Yb[CH($SiMe_3$)$_2$]. Sidebands are marked with asterisks. The feature around ~ -4 ppm should correspond to methyl groups whereas the remaining features correspond to aromatic resonances. (b) ^{29}Si NMR spectrum (500 MHz, spinning rate 30 kHz, RF field strength of $\nu_{1,max}$= 118 kHz and 10 ms recycle delay) of [O−2,6−tBu−C_6H_3]$_2$Yb[CH($SiMe_3$)$_2$]. Sidebands are marked with asterisks. The central band has a shift of −97.0 ppm.

References

(1) Steele, L. A. M.; Boyle, T. J.; Kemp, R. A.; Moore, C. The selective insertion of carbon dioxide into a lanthanide (III) 2, 6-di-t-butyl-phenoxide bond. *Polyhedron* **2012**, *42*, 258–264.

(2) Davidson, P. J.; Harris, D. H.; Lappert, M. F. Subvalent Group 4B metal alkyls and amides. Part I. The synthesis and physical properties of kinetically stable bis [bis (trimethysilyl) methyl]-germanium (II),-tin (II), and-lead (II). *J. Chem. Soc., Dalton Trans.* **1976**, 2268–2274.

(3) Walter, M. D.; Schultz, M.; Andersen, R. A. Weak paramagnetism in compounds of the type Cp'$_2$Yb(bipy). *New J. Chem.* **2006**, 238–246.

(4) Bain, G. A.; Berry, J. F. Diamagnetic Corrections and Pascal's Constants. *J. Chem. Educ.* **2008**, *85*, 532–536.

(5) Clément, R. J.; Pell, A. J.; Middlemiss, D. S.; Strobridge, F. C.; Miller, J. K.; Whittingham, M. S.; Emsley, L.; Grey, C. P.; Pintacuda, G. Spin-transfer pathways in paramagnetic lithium transition-metal phosphates from combined broadband isotropic solid-state MAS NMR spectroscopy and DFT calculations. *J. Am. Chem. Soc.* **2012**, *134*, 17178–17185.

(6) Kervern, G.; Pintacuda, G.; Zhang, Y.; Oldfield, E.; Roukoss, C.; Kuntz, E.; Herdtweck, E.; Basset, J.-M.; Cadars, S.; Lesage, A. Solid-state NMR of a paramagnetic DIAD-FeII catalyst: Sensitivity, resolution enhancement, and structure-based assignments. *J. Am. Chem. Soc.* **2006**, *128*, 13545–13552.

(7) Kervern, G.; Pintacuda, G.; Emsley, L. Fast adiabatic pulses for solid-state NMR of paramagnetic systems. *Chem. Phys. Lett.* **2007**, *435*, 157–162.

(8) Stoll, S.; Schweiger, A. EasySpin, a comprehensive software package for spectral simulation and analysis in EPR. *J. Magn. Reson.* **2006**, *178*, 42–55.

(9) Schosseler, P.; Wacker, T.; Schweiger, A. Pulsed ELDOR Detected NMR. *Chem. Phys. Lett.* **1994**, *224*, 319–324.

(10) Neese, F.; Wennmohs, F.; Becker, U.; Riplinger, C. The ORCA quantum chemistry program package. *J. Chem. Phys* **2020**, *152*, 224108.

(11) Perdew, J. P.; Ernzerhof, M.; Burke, K. Rationale for mixing exact exchange with density functional approximations. *J. Chem. Phys.* **1996**, *105*, 9982–9985.

(12) Becke, A. Density-functional thermochemistry. III. The role of exact exchange. *J. Chem. Phys* **1993**, *98*, 5648.

(13) Adamo, C.; Barone, V. Toward reliable density functional methods without adjustable parameters: The PBE0 model. *J. Chem. Phys.* **1999**, *110*, 6158–6170.

(14) Grimme, S.; Antony, J.; Ehrlich, S.; Krieg, H. A consistent and accurate ab initio parametrization of density functional dispersion correction (DFT-D) for the 94 elements H-Pu. *J. Chem. Phys* **2010**, *132*, 154104.

(15) Lenthe, E. v.; Baerends, E.-J.; Snijders, J. G. Relativistic regular two-component Hamiltonians. *J. Chem. Phys* **1993**, *99*, 4597–4610.

(16) Pantazis, D. A.; Neese, F. All-electron scalar relativistic basis sets for the lanthanides. *J. Chem. Theory Comput.* **2009**, *5*, 2229–2238.

(17) Weigend, F.; Ahlrichs, R. Balanced basis sets of split valence, triple zeta valence and quadruple zeta valence quality for H to Rn: Design and assessment of accuracy. *Physical Chemistry Chemical Physics* **2005**, *7*, 3297–3305.

(18) Stoychev, G. L.; Auer, A. A.; Neese, F. Automatic generation of auxiliary basis sets. *J. Chem. Theory Comput.* **2017**, *13*, 554–562.

(19) Neese, F. An improvement of the resolution of the identity approximation for the formation of the Coulomb matrix. *J. Comput. Chem.* **2003**, *24*, 1740–1747.

(20) Fdez. Galván, I.; Vacher, M.; Alavi, A.; Angeli, C.; Aquilante, F.; Autschbach, J.; Bao, J. J.; Bokarev, S. I.; Bogdanov, N. A.; Carlson, R. K., et al. OpenMolcas: From source code to insight. *J. Chem. Theory Comput.* **2019**, *15*, 5925–5964.

(21) Aquilante, F.; Autschbach, J.; Baiardi, A.; Battaglia, S.; Borin, V. A.; Chibotaru, L. F.; Conti, I.; De Vico, L.; Delcey, M.; Fdez. Galván, I., et al. Modern quantum chemistry with [Open] Molcas. *J. Chem. Phys.* **2020**, *152*, 214117.

(22) Roos, B. O.; Taylor, P. R.; Sigbahn, P. E. A complete active space SCF method (CASSCF) using a density matrix formulated super-CI approach. *Chem. Phys.* **1980**, *48*, 157–173.

(23) Andersson, K.; Malmqvist, P. A.; Roos, B. O.; Sadlej, A. J.; Wolinski, K. Second-order perturbation theory with a CASSCF reference function. *J. Phys. Chem.* **1990**, *94*, 5483–5488.

(24) Reiher, M. Douglas-Kroll-Hess Theory: a relativistic electrons-only theory for chemistry. *Theor. Chem. Acc.* **2006**, *116*, 241–252.

(25) Malmqvist, P. Å.; Roos, B. O.; Schimmelpfennig, B. The restricted active space (RAS) state interaction approach with spin–orbit coupling. *Chem. Phys. Lett.* **2002**, *357*, 230–240.

(26) Neese, F. Efficient and accurate approximations to the molecular spin-orbit coupling operator and their use in molecular g-tensor calculations. *J. Chem. Phys.* **2005**, *122*, 034107.

(27) Heß, B. A.; Marian, C. M.; Wahlgren, U.; Gropen, O. A mean-field spin-orbit method applicable to correlated wavefunctions. *Chem. Phys. Lett.* **1996**, *251*, 365–371.

(28) Heß, B. A.; Marian, C. M.; Wahlgren, U.; Gropen, O. A mean-field spin-orbit method applicable to correlated wavefunctions. *Chem. Phys. Lett.* **1996**, *251*, 365–371.

(29) Neese, F. Calculation of the zero-field splitting tensor on the basis of hybrid density functional and Hartree-Fock theory. *J. Chem. Phys.* **2007**, *127*, 164112.

(30) Roos, B. O.; Lindh, R.; Malmqvist, P.-Å.; Veryazov, V.; Widmark, P.-O. New relativistic ANO basis sets for transition metal atoms. *J. Phys. Chem. A* **2005**, *109*, 6575–6579.

(31) Roos, B. O.; Lindh, R.; Malmqvist, P.-Å.; Veryazov, V.; Widmark, P.-O.; Borin, A. C. New relativistic atomic natural orbital basis sets for lanthanide atoms with applications to the Ce diatom and LuF3. *J. Phys. Chem. A* **2008**, *112*, 11431–11435.

(32) Vancoillie, S.; Rulisek, L.; Neese, F.; Pierloot, K. Theoretical Description of the Structure and Magnetic Properties of Nitroxide- Cu (II)- Nitroxide Spin Triads by Means of Multiconfigurational Ab Initio Calculations. *J. Phys. Chem. A* **2009**, *113*, 6149–6157.

(33) Jung, J.; Islam, M. A.; Pecoraro, V. L.; Mallah, T.; Berthon, C.; Bolvin, H. Derivation of Lanthanide Series Crystal Field Parameters From First Principles. *Chem.Eur. J.* **2019**, *25*, 15112–15122.

(34) Kutzelnigg, W.; Fleischer, U.; Schindler, M. *Deuterium and shift calculation*; Springer, 1990; pp 165–262.

(35) London, F. Théorie quantique des courants interatomiques dans les combinaisons aromatiques. *J. phys. radium* **1937**, *8*, 397–409.

(36) Ditchfield, R. Self-consistent perturbation theory of diamagnetism: I. A gauge-invariant LCAO method for NMR chemical shifts. *Molecular Physics* **1974**, *27*, 789–807.

(37) Helgaker, T.; Jaszunski, M.; Ruud, K. Ab initio methods for the calculation of NMR shielding and indirect spin-spin coupling constants. *Chemical Reviews* **1999**, *99*, 293–352.

(38) Weinhold, F.; Landis, C. R.; Glendening, E. D. What is NBO analysis and how is it useful? *Int. Rev. Phys. Chem.* **2016**, *35*, 399–440.

(39) Glendening, E. D.; Landis, C. R.; Weinhold, F. NBO 7.0: New vistas in localized and delocalized chemical bonding theory. *J. Comput. Chem.* **2019**, *40*, 2234–2241.

(40) Kozlowski, D.; Pilme, J. New insights in quantum chemical topology studies using numerical grid-based analyses. *J. Comput. Chem.* **2011**, *32*, 3207–3217.

(41) Alessandri, R.; Zulfikri, H.; Autschbach, J.; Bolvin, H. Crystal Field in Rare-Earth Complexes: From Electrostatics to Bonding. *Chem.–Eur. J.* **2018**, *24*, 5538–5550.

(42) Sheldrick, G. M. A short history of SHELX. *Acta Crystallogr. Sect. A Found. Crystallogr.* **2008**, *64*, 112–122.

(43) Sheldrick, G. M. SHELXT - Integrated space-group and crystal-structure determination. *Acta Crystallogr. Sect. A Found. Crystallogr.* **2015**, *71*, 3–8.

(44) Sheldrick, G. M. Crystal structure refinement with SHELX. *Acta Crystallogr. Sect. C Struct. Chem.* **2015**, *71*, 3–8.

(45) Dolomanov, O. V.; Bourhis, L. J.; Gildea, R. J.; Howard, J. A. K.; Puschmann, H. OLEX2: a complete structure solution, refinement and analysis program. *J. Appl. Cryst.* **2009**, *42*, 339–341.

(46) Conley, M. P.; Lapadula, G.; Sanders, K.; Gajan, D.; Lesage, A.; Del Rosal, I.; Maron, L.; Lukens, W. W.; Coperet, C.; Andersen, R. A. The nature of secondary interactions at electrophilic metal sites of molecular and silica-supported organolutetium complexes from solid-state NMR spectroscopy. *J. Am. Chem. Soc.* **2016**, *138*, 3831–3843.

(47) Gordon, C. P.; Shirase, S.; Yamamoto, K.; Andersen, R. A.; Eisenstein, O.; Copéret, C. NMR chemical shift analysis decodes olefin oligo- and polymerization activity of d^0 group 4 metal complexes. *Proc. Natl. Acad. Sci. USA* **2018**, *115*, 5867–5876.

(48) Ashuiev, A.; Allouche, F.; Wili, N.; Searles, K.; Klose, D.; Copéret, C.; Jeschke, G. Molecular and supported Ti(III)-alkyls: efficient ethylene polymerization driven by the π-character of metal-carbon bonds and back donation from a singly occupied molecular orbital. *Chem. Sci.* **2021**, *12*, 780–792.

(49) Moon, S.; Patchkovskii, S. *Calculation of NMR and EPR Parameters*; John Wiley & Sons, Ltd, 2004; Chapter 20, pp 325–338.

(50) Pennanen, T. O.; Vaara, J. Density-functional calculations of relativistic spin-orbit effects on nuclear magnetic shielding in paramagnetic molecules. *J. Chem. Phys.* **2005**, *123*, 174102.

(51) Pennanen, T. O.; Vaara, J. Nuclear magnetic resonance chemical shift in an arbitrary electronic spin state. *Phys. Rev. Lett.* **2008**, *100*, 133002.

(52) Vaara, J.; Rouf, S. A.; Mares, J. Magnetic couplings in the chemical shift of paramagnetic NMR. *J. Chem. Theory Comput.* **2015**, *11*, 4840–4849.

(53) Van den Heuvel, W.; Soncini, A. NMR chemical shift in an electronic state with arbitrary degeneracy. *Physical review letters* **2012**, *109*, 073001.

(54) Van den Heuvel, W.; Soncini, A. NMR chemical shift as analytical derivative of the Helmholtz free energy. *The Journal of chemical physics* **2013**, *138*, 054113.

(55) Ramsey, N. F. Magnetic shielding of nuclei in molecules. *Phys. Rev.* **1950**, *78*, 699.

(56) Wolinski, K.; Hinton, J. F.; Pulay, P. Efficient implementation of the gauge-independent atomic orbital method for NMR chemical shift calculations. *J. Am. Chem. Soc.* **1990**, *112*, 8251–8260.

(57) Lang, L.; Ravera, E.; Parigi, G.; Luchinat, C.; Neese, F. Solution of a Puzzle: High-Level Quantum-Chemical Treatment of Pseudocontact Chemical Shifts Confirms Classic Semiempirical Theory. *J. Phys. Chem. Lett.* **2020**, *11*, 8735–8744.

(58) Gerloch, M.; Miller, J. R. *Progress in Inorganic Chemistry*; John Wiley & Sons, Inc., 1968; Vol. 10; pp 1–47.

(59) Orchard, A. F. *Magnetochemistry*; Oxford University Press, 2003.

(60) Gerloch, M.; Mackey, D. J. Single-crystal magnetic properties of lanthanide complexes. Part I. Tri-iodohexakis (antipyrine) ytterbium. *J. Chem. Soc. A* **1970**, 3030–3040.

(61) Edelstein, N. M. *Organometallics of the f-Elements*; Springer, 1979; pp 37–79.

(62) Walter, M. D.; Matsunaga, P. T.; Burns, C. J.; Maron, L.; Andersen, R. A. Synthesis and Reactions of $[Cp^{\star}_2Yb]_2(\mu\text{-Me})$ and $[Cp^{\star}_2Yb]_2(\mu\text{-Me})(Me)$ and Related Yb_2(II, III) and Yb_2 (III, III) Compounds. *Organometallics* **2017**, *36*, 4564–4578.

(63) Schulz, H.; Reddmann, H.; Amberger, H.-D.; Kanellakopulos, B.; Apostolidis, C.; Rebizant, J.; Edelstein, N. M. Zur Elektronenstruktur metallorganischer Komplexe der f-Elemente: LI. Synthese, Kristall-, Molekül- und Elektronenstruktur von $Cp_3Nd(NCCH_3)_2$. *J. Organomet. Chem.* **2001**, *622*, 19–32.